DOT/FAA/AR-05/31

Office of Aviation Research
Washington, D.C. 20591

Feasibility Study of Thermal-Elastographic Detection of Nonvoided Hard Alpha Inclusions in Titanium Alloys

September 2005

Final Report

This document is available to the U.S. public
through the National Technical Information Service (NTIS),
Springfield, VA 22161.

U.S. Department of Transportation
Federal Aviation Administration

NOTICE

This document is disseminated under the sponsorship of the U.S. Department of Transportation in the interest of information exchange. The United States Government assumes no liability for the contents or use thereof. The United States Government does not endorse products or manufacturers. Trade or manufacturer's names appear herein solely because they are considered essential to the objective of this report. This document does not constitute FAA certification policy. Consult your local FAA aircraft certification office as to its use.

This report is available at the Federal Aviation Administration William J. Hughes Technical Center's Full-Text Technical Reports page: actlibrary.tc.faa.gov in Adobe Acrobat portable document format (PDF).

Technical Report Documentation Page

1. Report No.	2. Government Accession No.	3. Recipient's Catalog No.
DOT/FAA/AR-05/31		

4. Title and Subtitle	5. Report Date
FEASIBILITY STUDY OF THERMAL-ELASTOGRAPHIC DETECTION OF NONVOIDED HARD ALPHA INCLUSIONS IN TITANIUM ALLOYS	September 2005
	6. Performing Organization Code
7. Author(s)	8. Performing Organization Report No.
Waled Hassan*, Jim Hall*, Fred Vensel*, Peter Nagy**, and Kevin Kramer**	
9. Performing Organization Name and Address	10. Work Unit No. (TRAIS)
*Honeywell Engines, Systems & Services Phoenix, Arizona **University of Cincinnati Cincinnati, Ohio	11. Contract or Grant No. DTFA03-020C-00045
12. Sponsoring Agency Name and Address	13. Type of Report and Period Covered
U.S. Department of Transportation Federal Aviation Administration Office of Aviation Research Washington, DC 20591	Final Report
	14. Sponsoring Agency Code ANE-110

15. Supplementary Notes

The FAA William J. Hughes Technical Center Technical Monitors were Paul Swindell and Cu Nguyen.

16. Abstract

Hard alpha or high interstitial defects (HID), often and erroneously referred to as low-density inclusions (type I) in titanium alloys, have been the focus of attention off and on since the application of titanium to rotating components in gas turbine aeroengines. There have been a number of failures due to hard HIDs that were not voided in critical engine rotating components; they escaped the quality assurance net of testing centered on some variant of ultrasonic inspection with focus on detection of internal interfaces such as voids, or microcracks. The objective of this research was to investigate the feasibility of a new ultrasonic nondestructive test method aimed at detecting hard alpha inclusions in titanium billets. The method is based on the basic principle of elastography, a recently developed imaging technique that can detect both soft and hard inclusions in a highly heterogeneous medium inclusions, which are highly inhomogeneous themselves. According to the proposed modified elastographic approach, heating the specimen produces the local strain. The observed shift in the grain speckle is, therefore, a combination of the increasing propagation distance caused by thermal expansion and the decreasing sound velocity caused by the temperature dependence of the sound velocity. In this case, the relevant physical contrast mechanism is mainly thermal rather than solely elastic. Based on the measurements conducted during the research, it was established that the acoustothermal coefficient is the dominating factor and is an order of magnitude higher than the effect of the acoustoelastic and thermal expansion coefficients. Although the feasibility of such a technique was established based on the property measurements in titanium nitride specimens (synthetic hard alpha) and using simulation tools, the lack of appropriate naturally occurring, unvoided hard alpha inclusion specimens rendered a complete laboratory demonstration impossible under the program. Should such specimens become available, it would be straightforward to verify feasibility in future efforts.

17. Key Words	18. Distribution Statement
Hard alpha inclusions, Nonvoided hard alpha inclusions, Ultrasonic testing, Elastography, Thermal elastography, Billet inspection, Thermal expansion coefficient, Acoustothermal coefficient, Acoustoelastic coefficient, Longitudinal velocity, Shear velocity	This document is available to the public through the National Technical Information Service (NTIS) Springfield, Virginia 22161.

19. Security Classif. (of this report)	20. Security Classif. (of this page)	21. No. of Pages	22. Price
Unclassified	Unclassified	60	

Form DOT F1700.7 (8-72) Reproduction of completed page authorized

TABLE OF CONTENTS

		Page
EXECUTIVE SUMMARY		ix
1.	INTRODUCTION	1
1.1	Purpose	2
1.2	Background	2
1.3	Technical Approach	4
2.	SPECIMENS	8
2.1	Synthetic TiN Material	8
2.2	Synthetic Inclusions (TiN) Embedded in Ti-6Al-4V Block	10
2.3	Naturally Occurring Voided Hard Alpha Inclusions	11
3.	EXPERIMENTAL SETUP FOR MEASUREMENT OF THE THREE NONLINEAR PARAMETERS	17
3.1	Thermal Expansion Coefficient Measurements	17
3.2	Acoustoelastic Coefficient Measurements	18
3.3	Acoustothermal Coefficient Measurements	20
4.	RESULTS FROM THE EXPERIMENTAL MEASUREMENTS OF THE THREE NONLINEAR PARAMETERS	21
4.1	Thermal Expansion Coefficient	21
4.2	Acoustoelastic Coefficient	24
4.3	Acoustothermal Coefficient	28
5.	RELATIVE CONTRIBUTIONS TO THE OVERALL THERMAL EFFECT	32
6.	VELOCITY MEASUREMENTS	33
7.	NUMERICAL SIMULATION FOR PRELIMINARY FEASIBLITY ASSESSEMENT	34
8.	FURTHER ANALYSIS OF DEFECT X	39
8.1	Eddy-Current and Acoustic Microscopy Imaging	39
8.2	Metallurgical and Microprobe Analysis	41
9.	SUMMARY	46
10.	RECOMMENDATIONS	49
11.	REFERENCES	50

LIST OF FIGURES

Figure		Page
1	Forging and Billet Inspectability Comparison	3
2	Micrograph of a Nonvoided HID	4
3	Synthetic TiN Specimens as Received and Before Cutting	8
4	Synthetic TiN Specimens After Cutting Into 0.22- by 0.38- by 1.0-inch Parallelepiped Specimens	9
5	Billet and Forging Ti-6Al-4V Specimens After Cutting Into 0.22- by 0.38- by 1.0-inch Parallelepiped Specimens	9
6	Ti-6Al-4V Specimen With Three Cylindrical Synthetic TiN Inclusions	10
7	Peak Reflected Amplitude C-Scan Images of the Ti-6Al-4V With Synthetic Cylindrical Inclusions With the UT Transducer Focused at (a) the Diffusion Bond Line and (b) the Tip of the Cylinders With Axes Perpendicular to the Diffusion Bond Line	11
8	Locations of Defects X and D in the Billet B2W2C	12
9	Two Blocks Containing Defects X and D	13
10	C-Scan Images of Defect X	13
11	Time of Flight Data for Defect X	14
12	C-Scan Images of Defect D	14
13	Time of Flight Data for Defect D	15
14	C-Scan Images of the Block Containing Defect X	15
15	Time of Flight Data for the Block Containing Defect X	16
16	C-Scan Images of the Block Containing Defect D	16
17	Time of Flight Data for the Block Containing Defect D	17
18	Schematic Diagram of the TEC Measurements	18
19	Experimental Setup for TEC Measurements	18
20	Schematic Diagram of the AEC Measurements	19

21	Experimental Setup for AEC Measurements	19
22	Schematic Diagram of the ATC Measurements	20
23	Experimental Setup for ATC Measurements	20
24	Percent Linear Change vs Temperature for Titanium With Varying Levels of Nitrogen Content	23
25	The ACE vs Temperature for Titanium With Varying Levels of Nitrogen Content	23
26	Relative Velocity Change vs Stress in Al-2024 Using a Longitudinal Transducer	26
27	Relative Velocity Change vs Stress in Al-2024 Using a Shear Transducer	26
28	Relative Velocity Change vs Stress in Ti-6Al-4V Using a Longitudinal Transducer	27
29	Relative Velocity Change vs Stress in Ti-6Al-4V Using a Shear Transducer	27
30	Apparent Velocity Change vs Temperature in Titanium With 3.1% N Using a Longitudinal Transducer (Acceptable Data)	29
31	Apparent Velocity Change vs Temperature in Titanium With 3.1% N Using a Longitudinal Transducer (Unacceptable Data)	30
32	Distribution of the Coefficient of Determination (R^2) vs the Longitudinal ATC (β)	31
33	Representation of the Longitudinal ATC Data Listed in Table 3	31
34	Longitudinal Velocity in Titanium With Varying Levels of N Content	34
35	Shear Velocity in Titanium With Varying Levels of N Content	34
36	A Numerical Simulation Model Setup	35
37	Simulation Results for a Cigar-Shaped Inclusion 15 mm Long and 4 mm Wide	36
38	Analysis of the Time Shift in the Peak Due to Sound Speed Modulation in the Inclusion for the Scenarios Depicted in Figure 37	37
39	The TOF and Reflected Peak Amplitude Scans for Defect X	37
40	Simulation Results for a Cigar-Shaped Inclusion 15 mm Long and 1 mm Wide	38
41	Slicing Process Performed on Defect X Perpendicular to its Axis to Produce Twenty 100-mil Slices With 15-mil Gaps	39

42	Sample Results of the Eddy-Current Imaging of Some of the Slices From Inclusion X	40
43	Sample Results of the Acoustic Microscopy Imaging of Some of the Slices From Inclusion X	41
44	Microstructure for Slice 13 Showing the Nonuniform Thickness Along the Width of About 8 mm	42
45	Higher Magnification View of Area Circled in Figure 44	42
46	High Magnification, Backscattered Electron Image of Mottled Area Seen in Figure 45, Highlighting Areas Where Energy Dispersive X-Ray Analyses Were Made	43
47	Nitrogen Composition Trace (From Microprobe Analysis) Across Defect of Slice 13 Along Profile 1	44
48	Microprobe Trace Also From Slice 13 Along Profile 2 Showing Much Higher N Content Than the First Trace	44
49	Combined Traces of N and Al for Slice 13 Along Profile 2	45

LIST TABLES

Table		Page
1	The PLC and ACE of Ti-6Al-4V Directional (Textured) Specimens	22
2	The PLC and ACE of Titanium Specimens With Varying Levels of Nitrogen	23
3	Measured Average ATCs Using a 5-MHz Longitudinal Transducer	29
4	Measured Average ATCs Using a 5-MHz Shear Transducer	29
5	Size of the Defect in Each Examined Slice Cross Section	41
6	Qualitative Differences in Composition With Respect to the Base Alloy Composition	45

LIST OF ACRONYMS

A/D	Analog to digital
ACE	Average coefficient of expansion
AEC	Acoustoelastic coefficient
Al	Aluminum
ATC	Acoustothermal coefficient
C	Carbon
CBS	Contaminated Billet Study
D/A	Digital to analog
DCE	Differential coefficient of expansion
EDX	Energy dispersive x-ray analysis
ETC	Engine Titanium Consortium
FAA	Federal Aviation Administration
FBH	Flat-bottom hole
GE GRC	GE Global Research Center
GE	General Electric
HID	High interstitial defects
HIP	Hot isostatic press
LVDT	Linear variable differential transducer
MTS	Material test system
MZI	Multizone inspection
N	Nitrogen
NDE	Nondestructive evaluation
NDT	Nondestructive test
Nsec	Nanoseconds
O	Oxygen
OEM	Original equipment manufacturer
PLC	Percent linear change
SNR	Signal-to-noise ratio
SRS	Stanford Research Systems, Inc.
TEC	Thermal expansion coefficient
TIC	Time interval counter
TiN	titanium nitride
TOF	Time of Flight
TRMD	Turbine Rotor Material Design
UT	Ultrasonic
VAR	Vacuum arc remelting
WPAFB	Wright-Patterson Air Force Base

EXECUTIVE SUMMARY

Hard alpha or high interstitial defects (HID) often, and erroneously, referred to as low-density inclusions (type I) in titanium alloys, have been the focus of attention off and on since the application of titanium to rotating components in gas turbine aeroengines. There have been failures of components and, unfortunately, some loss of life associated with the presence of such defects and a concomitant-reduced fatigue life. The early characterization of this class of defects resulted in identifying a few key characteristics that are responsible for the reduced fatigue life of titanium components that contain them. Chief amongst these characteristics is a higher hardness than the nominal alloy due to interstitial (nitrogen, carbon, and oxygen) alloying at levels much higher than the nominal alloy. Besides being hard and brittle, these nuggets of high interstitial stabilization are refractory, relative to the melting temperature for the host titanium alloy, and are slow to dissolve. This refractory nature, combined with the size of the initial seed, may permit the nugget to survive, with its hardness characteristics, all the vacuum arc remelting (VAR) process steps normally used to create a titanium ingot. This realization resulted in the institution of triple VAR to replace the standard double VAR for premium-grade applications, resulting in a significant reduction in occurrence of hard alpha defects.

Recently, ultrasonic technology for the detection of internal discontinuities, such as voids and microcracks, has made significant improvements. However, there have been a small number of recognized failures due to HIDs that were not voided in critical engine rotating components. Obviously, they had escaped the quality assurance net of testing centered on some variant of ultrasonic inspection with focus on detection of internal interfaces such as voids, or microcracks; HIDs must be recognized as the most insidious of the hard alpha defects.

The objective of this research was to investigate the feasibility of a new ultrasonic nondestructive test method aimed at detecting hard alpha inclusions in titanium billets. The method was based on the basic principle of elastography, a recently developed imaging technique that can detect both soft and hard inclusions in a highly heterogeneous medium, inclusions that are highly inhomogeneous themselves. According to the proposed modified elastographic approach, heating the specimen produces the local strain. The observed shift in the grain speckle is then a combination of the increasing propagation distance caused by thermal expansion and the decreasing sound velocity caused by the temperature dependence of the sound velocity. In this case, the relevant physical contrast mechanism is mainly thermal rather than solely elastic.

Based on the measurements conducted during the research using different samples, it was established that the acoustothermal coefficient was the dominating factor and was an order of magnitude higher than the effect of the acoustoelastic and thermal expansion coefficients. Although the feasibility of this inspection technique was established based on the properties measurements in titanium nitride specimens (synthetic hard alpha) and using simulation tools, the lack of appropriate naturally occurring, unvoided hard alpha inclusion specimens rendered a complete laboratory demonstration impossible under the program. Should such specimens become available, it would be straightforward to verify feasibility in future efforts.

1. INTRODUCTION.

Hard alpha or high interstitial defects (HID), often and erroneously referred to as low-density inclusions (type I) in titanium alloys, have been the focus of attention off and on since the application of titanium to rotating components in gas turbine aeroengines. There have been failures of components and, unfortunately, some loss of life associated with the presence of such defects and a concomitant-reduced fatigue life [1-3].

Early characterization of this class of defects resulted in identifying of a few key characteristics that were responsible for reduced fatigue life of titanium components that contain them [4-6]. Chief amongst these characteristics was a higher hardness than the nominal alloy due to interstitial (nitrogen (N), carbon (C), and oxygen (O)) alloying at levels much higher than the nominal alloy. Hence, the descriptive name, high interstitial defect. Besides being hard and brittle, these nuggets of high interstitial stabilization were refractory, relative to the melting temperature for the host titanium alloy, and are slow to dissolve. This refractory nature, combined with the size of the initial seed, may permit the nugget to survive, with its hardness characteristics, all the vacuum arc remelting (VAR) process steps normally used to create a titanium ingot. This realization resulted in the institution of triple VAR to replace the standard double VAR for premium-grade applications, resulting in a significant reduction in occurrence of hard alpha defects.

Most of the finds of HIDs were associated with internal voids or cracks that facilitated their detection by ultrasonic (UT) test methods. This led to the refinement of UT techniques in attempts to detect smaller and smaller voids or internal flaws associated with most HIDs. The industry responded with improved UT technology, including multizone inspection (MZI), and with improved titanium manufacturing and quality controls to reduce, significantly, the occurrence of hard alpha defects [7]. While the incidence of HIDs has become quite small, it remains finite. Furthermore, the probability of detection, or more to the point, the probability of missing a finite hard alpha defect in the combination of billet and forging inspections is still high enough to cause concern.

The detection technology for finding (not missing) defects with associated voids or cracks has improved and has been the focus of a great deal of attention in recent years. Currently, there is redundant UT inspection in rotor material. First, there is the billet inspection followed by an inspection of the finished forging that has been made oversized and machined to a shape (sonic shape) that lends itself to maximum inspectability. In the period of time that UT technology for the detection of internal discontinuities, such as voids and microcracks has made significant improvements, there have been a small number of recognized failures due to hard alphas (HIDs) that were not voided. Obviously, they had escaped the quality assurance net of testing centered on some variant of UT inspection with focus on detection of internal interfaces such as voids or microcracks, which must be recognized as the most insidious of the hard alpha defects.

This report outlines the results of a feasibility study that was aimed at investigating the possibility of using a rather new approach for the detection of nonvoided, hard alpha inclusions in titanium alloys. The technique is based on the basic principle of elastography, a recently developed imaging technique that can detect both soft and hard inclusions in a highly

heterogeneous medium, which are highly inhomogeneous themselves. This will lead to means of improved detectability and characterization of such defects using UT technology.

1.1 PURPOSE.

The objective of this research was to investigate the feasibility of a new UT nondestructive test (NDT) method aimed at detecting nonvoided hard alpha inclusions in titanium billets. The method is based on the basic principle of elastography, a recently developed imaging technique that can detect both soft and hard inclusions in a highly heterogeneous medium, which are highly inhomogeneous themselves.

1.2 BACKGROUND.

The quality level in the manufacture of rotor-grade titanium materials for propulsion turbine engine applications has significantly improved over the past decade and a half, partially due to the efforts sponsored by the Federal Aviation Administration (FAA) following the Sioux City, Iowa, crash. While the implementation of strict foundry controls and improved processing techniques such as cold hearth and triple melting have significantly reduced the rate of defects present in titanium products, there is still room for error in these processes, which may manifest itself in terms of latent defects in the volume of the final product. The engine manufacturers guard against these latent defects with a redundant set of UT inspections, one applied to the billet and another applied to each forging manufactured from the billet.

There remains a disagreement in the engine community on the best practices for the implementation of billet and forging inspections on rotor-grade titanium. Some believe that a screen of the billet to a #2 to #5 flat-bottom hole (FBH) sensitivity is adequate provided the inspection on the final forging is more stringent in order to safeguard against such latent defects that may have been missed in the billet. Others in the industry believe that latent defects, which remain undetected in the billet, may be stretched or pushed into areas within the forging, which may result in a lower probability of detection.

A joint Engine Titanium Consortium (ETC) and turbine rotor material design (TRMD) effort investigated the impact of processing naturally occurring and synthetic defects on UT inspection detectability in the recent past [8]. For the efforts involving naturally occurring defects, the team selected three billet segments from the Contaminated Billet Study (CBS) material, ultrasonically characterized the defects in the billet stage, subsequently forged the billet segments, and again, ultrasonically characterized the forging shapes. While the data was quite sparse and all the forging processing was done isothermally, the results of this exercise clearly demonstrated that the detectability of a given defect changes dramatically as a result of the forging processing. Figure 1 illustrates a forging and billet inspectability comparison. The solid line on the graph represents a 1:1 correlation in defect detectability. This figure was published by TRMD and includes data from billet, pancake forging, semifinished forgings, dogbone, and backflow forgings. It clearly indicates that nearly all of the HID defects are much more detectable in the billet than in the subsequent forging shapes.

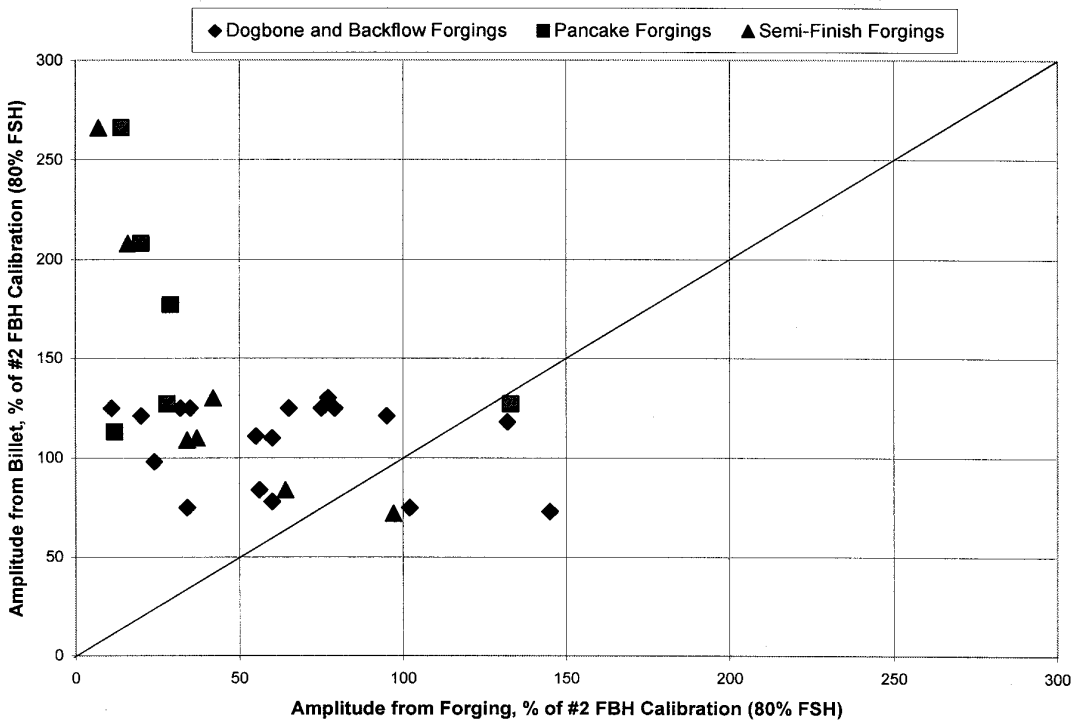

FIGURE 1. FORGING AND BILLET INSPECTABILITY COMPARISON

Another CBS effort investigated the impact of healing a defect on the UT detectability [6]. This effort was undertaken for two reasons: (1) to investigate the feasibility of manufacturing a nonvoided hard alpha inclusion using this process and (2) to investigate the impact of the void closure on the UT inspection process. For this investigation, the team used a billet segment with an indication approximately equivalent to a #3 FBH, as detected by conventional billet inspection (100% amplitude with a signal-to-noise of 2.9), this billet segment was then hot isostatic press (HIP)ped at a subtransus temperature, time, and pressure consistent with industry convention for this alloy. The HIPped segment was then re-inspected to investigate the resultant impact. No indications were observed in the post-HIPped sample, demonstrating that the process effectively closed the voids and that detection of nonvoided hard alphas requires additional investigation.

The importance of understanding and maintaining strict process control and the need for robust, highly accurate inspection techniques became evident on several occasions over the past couple of years. Nearly 6 years ago, a titanium melter received silica material extensively contaminated with pure tungsten wire pieces. These contaminates were discovered during the processing of rotor-grade Ti-6-2-4-2. The result of this quality escape was the contamination of 22 heats of rotor-grade material (approximately 190,000 lb or > 2,500 engine parts) allocated for engine builds. Fortunately, this material did not make it to engines, as some of the material was multizone inspected and all 22 heats of the associated material were downgraded. In excess of 100 individual tungsten inclusions were discovered in the billet using MZI, a technique that is more sensitive than the conventional billet inspection. Furthermore, upon subsequent evaluation,

it was discovered that none of these defects would be rejectable using industry standard, conventional billet UTs. Two questions immediately come to mind when formulating risk assessment for components manufactured from associated material: (1) Would have any of these defects (and any other defects that were missed by MZI) been machined away or detected in the forging? (2) If any of these defects made it to the final product in a critical location, would they be detrimental to component operation?

More recently, another titanium melter reported a higher than typical rate of hard alpha finds in the manufacture of its rotor-grade titanium. Four hard alpha inclusions were discovered over a 3-month period, which amounts to approximately a 6 times increase in the typical rate of hard alpha detection. This resulted in a cascading effect through the industry. When supplies are short, this places an additional strain on the availability of rotor-grade alloy. This occurrence, and the associated reactions by original equipment manufacturers (OEM), pointed out that while engine manufacturers have high confidence in the UT inspection technique, the presence of nonpreferentially oriented defects and nonvoided hard alpha inclusions make detection more difficult. In fact, there have been some failures associated with nonvoided hard alpha defects. Figure 2 is an actual photomicrograph of one such defect. It remained nondetected in both the billet and the forging inspection. Current technology allows these sort of defects to escape and here-in lies a most serious challenge to UT technology. There is a keen awareness of the potential consequences of a hard alpha defect (HID) escaping into a fielded part, therefore, very costly precautionary measures are taken.

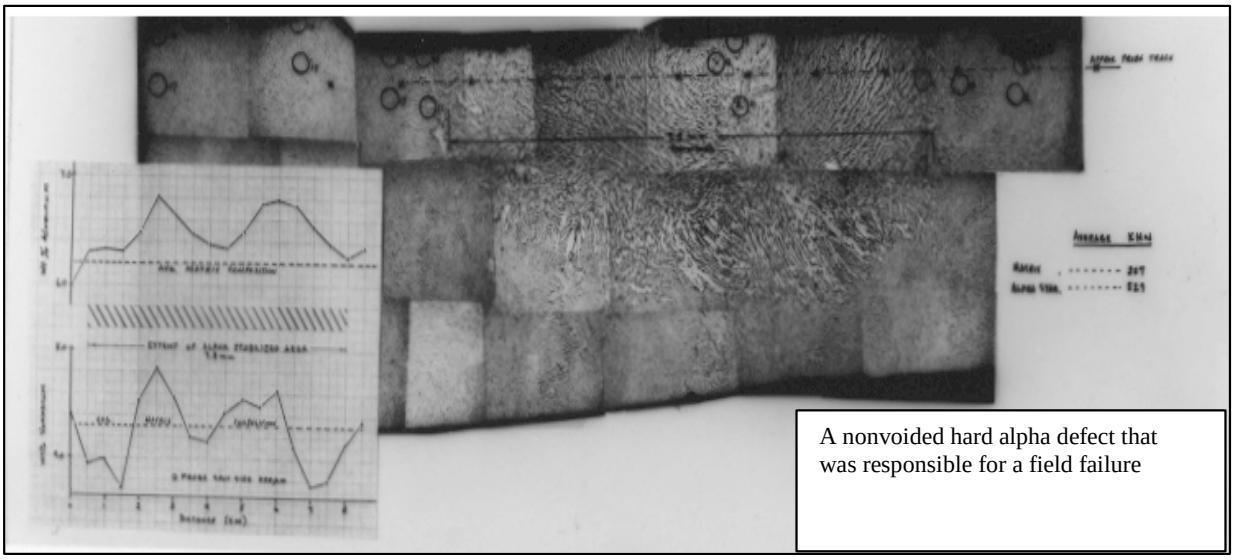

FIGURE 2. MICROGRAPH OF A NONVOIDED HID

1.3 TECHNICAL APPROACH.

Hard alpha inclusions are low-density, hard, brittle regions of spuriously high nitrogen and oxygen content that occur in titanium alloys. These inclusions are often cracked or include voids, which makes it much easier to detect them by conventional NDT methods, including UT backscattering. However, the detection of uncracked or unvoided hard alpha inclusions

represents a very significant challenge for UT NDT. Although every weight percent of nitrogen was found to increase the sound velocity by roughly 3% [9], the absolute acoustic impedance contrast is expected to be substantial (10%-15%), the actual signal-to-noise ratio (SNR) is badly limited by three adverse effects: (1) the nitrogen content varies gradually towards the center of the inclusion; therefore, the reflected signal remains rather weak, (2) the shape of the inclusion is typically very irregular; therefore, the flaw signal is further reduced by random geometrical scattering effects, and (3) the competing grain noise is frequently very high because of the often coarse microstructure of the surrounding material. As a result, the backscattered UT signal from the unvoided hard alpha inclusion is usually indistinguishable from the incoherent material noise based on its strength alone and the probability of its detection remains inherently low.

The objective of this program was to investigate the feasibility of a new UT NDT method aimed at detecting nonvoided hard alpha inclusions in titanium billets. As a working hypothesis, it was postulated that, in general, nonlinear elastic properties are more sensitive to the presence of interstitial (N, C, and O) elements that led to higher hardness than the corresponding linear elastic properties. Although this assumption can be supported by a great variety of observations in similar cases, there is no evidence at this point that the nonlinear contrast between a typical hard alpha inclusion with respect to the surrounding titanium alloy is actually higher than the better-known linear contrast. One of the primary goals of the program was to determine how different nonlinear material properties are affected by increasing nitrogen content.

There are a great variety of nonlinear elastic parameters that could be exploited for nondestructive evaluation (NDE) of hard alpha inclusions. The three nonlinear parameters that were investigated in detail were chosen with special regard to the particular nonlinear NDE method to be used in this study, namely, thermally activated elastography. These nonlinear parameters include the thermal expansion coefficient (TEC), the thermal coefficient of sound velocity acoustothermal coefficient (ATC), and the stress coefficient of sound velocity acoustoelastic coefficient (AEC). Of course, these nonlinear parameters are mutually interrelated and are all-dependent on the higher-order elastic moduli of the material.

One of the most obvious manifestations of elastic nonlinearity in solids is the existence of thermal expansion due to the nonparabolic nature of the atomic potential. Since the potential well is tilted outward, the nearest neighbors will separate from each other more at higher temperatures when they oscillate more around their equilibrium position. Another well-known manifestation of the same elastic nonlinearity is the effect of material deformation on the propagation velocity of acoustic waves. Regardless whether the strain is caused by stress (elastic strain) or temperature variation (thermal strain), the changing sound velocity is not only a sensitive indication but also a reliable, quantitative measure of material nonlinearity. All these parameters are related to the third- and higher-order elastic constants of the material and can be readily measured as functions of the fractional density of contaminating interstitial elements. It should be noted that other nonlinear phenomena, such as the generation of second and higher harmonics by finite amplitude acoustic waves propagating through the material, could also be readily used for studying the nonlinear contrast produced by variations in interstitial contamination, but the three parameters described above bear direct relevance to the NDE procedure of interest in this program.

Three important basic tasks within the current feasibility study were aimed at experimentally determining the (1) TEC, (2) the AEC, and (3) the ATC of titanium alloy coupons of varying interstitial (N) content. These measurements were conducted in the NDE Laboratory of the University of Cincinnati and provided the basic information for subsequent determination of the dominating factor of the previously mentioned effects in the development of a special thermally activated elastographic inspection method for the detection of nonvoided hard alpha inclusions. All three parameters will play a role in the formation of a nonlinear contrast between the inclusion and the surrounding host material. Due to the presence of substantial differences in nonlinear material properties, when the material is heated to elevated temperatures, (1) the sound velocity in the inclusion changes with respect to the host, (2) the inclusion expands with respect to the host, and (3) it also develops thermal stresses that again affect the sound velocity. It was expected that these three nonlinear effects combine with each other to produce an even more substantial overall nonlinear contrast. In particular, the effective propagation delays between scattering grains increase not only because of thermal expansion, but also because the sound velocity decreases—partly because of the direct effect of the increased temperature and partly because of the development of thermal stresses. However, the actual measurements revealed that the ATC is the dominating effect and the other two factors, for all practical purposes, can be ignored as will be detailed in a later section.

To effectively conduct this program, the need for samples and specimens that represent a naturally occurring unvoided hard alpha could not be overemphasized. The following represents a summary of the samples that were made available to the program:

- Synthetic material of titanium nitride (TiN) with various nitrogen content which is the widely accepted simulation of hard alpha inclusions from an UT properties point of view. These specimens were used for properties measurements (obtained from the NDE branch at Wright-Patterson Air Force Base (WPAFB) and made by GE Global Research Center (GE GRC)).

- Synthetic inclusions (TiN) with various nitrogen content embedded in Ti-6Al-4V block for inspection validation (obtained from the NDE Branch WPAFB and made GE GRC). These specimens were tested to evaluate how representative they are to a naturally occurring hard alpha inclusion in Ti-6Al-4V.

- Naturally occurring, voided hard alpha inclusions from the CBS billet material (obtained from the ETC). These specimens were HIPped to heal and evaluated to assess how representative they would be to a naturally occurring, nonvoided hard alpha inclusion in Ti-6Al-4V. These specimens were intended for validating the proposed thermal-elastographic technique.

More details on these specimens will be presented.

The main deliverable result of this feasibility study was the above described experimental study of the nonlinear contrast mechanism between a hard alpha inclusion and a titanium alloy host. However, a series of preliminary experiments were also proposed to illustrate the feasibility of one particular nonlinear inspection method that has the potential of being sufficiently sensitive to detect the nonlinear contrast of nonvoided hard alpha inclusions. The method was based on the

basic principle of elastography, a recently developed imaging technique that can detect both soft and hard inclusions in a highly heterogeneous medium, which are highly inhomogeneous themselves. Under these conditions, conventional sonography, based on the strength of UT backscattering alone, cannot be used to detect the inclusion with the required high level of confidence. In relatively compliant soft tissue, sufficient local displacements can be produced by a quasi-static external stress field so that local strains and, thereby, the local elastic stiffness, can be estimated from differential UT speckle displacements. The processed strain image is called an elastogram that has been shown to offer dramatically better detectability of scattering inclusions than the conventional sonogram itself. This technique has been primarily aimed at biomedical diagnostic applications where the elastic deformation is both substantial and easy to produce.

A similar elastographic approach, based on external deformation of large pieces of structural metals like a Ti-6Al-4V billet, would require tremendous external forces and would still result in minuscule contrast because, as indicated by the mere 10%-15% variation in sound velocity, the elastic stiffness of the brittle inclusion was only about 20%-30% higher than the surrounding intact material. According to the proposed modified elastographic approach, the local strain was produced by heating the specimen. The observed shift in the grain speckle was, therefore, a combination of the increasing propagation distance caused by thermal expansion and the decreasing sound velocity caused by the temperature dependence of the sound velocity (these two effects are actually related through the elastic nonlinearity of the material). Although the absolute change in propagation time due to the thermal strain and the temperature dependence of the sound velocity is probably comparable to what one could achieve by external mechanical loading as a result of the corresponding elastic strain and the stress dependence of the sound velocity, the thermal loading method is inherently simpler. More importantly, the relevant physical contrast mechanism is thermal rather than elastic. This contrast mechanism has never been investigated before in the scientific literature. However, indirect evidence available in the published literature as well as these measurements suggest that the variation in thermal velocity coefficient are substantially, probably as much as one order of magnitude, stronger than in the corresponding elastic coefficients. This is not surprising based on the fact that the nitrogen and oxygen contamination induced hardening and embrittlement is a nonlinear rather than linear effect on the mechanical properties of the material. In summary, the proposed technical approach included:

- acquiring Ti-6Al-4V specimens containing nonvoided hard alpha inclusions (for technique validation) and TiN specimens with various nitrogen content (for hard alpha properties measurements).

- characterizing the three nonlinear coefficients that most likely will play a role in this phenomenon, namely, TEC, ATC, and AEC.

- experimentally evaluating the relative effect of heating on the deformation of hard alpha inclusions and titanium alloys.

- developing the algorithm needed to extract the thermal-elastogram from the corresponding sonogram and setup experiments for this purpose.

- demonstrating the technique on the acquired Ti-6Al-4V specimens with hard alpha inclusions.

- preparing and reporting the results of the feasibility study.

The following sections detail the results, limitations, and conclusions based on the activities that occurred under this program.

2. SPECIMENS.

As mentioned in section 1.3, three different types of samples and specimens were obtained to facilitate the performance of the program. The following is a detailed description of these samples.

2.1 SYNTHETIC TiN MATERIAL.

These specimens were obtained from the NDE branch at WPAFB and were originally made by GE GRC. The TiN samples were prepared by three techniques: (1) HIP consolidation of blended titanium and TiN powders, (2) arc melting of titanium sponge in an N-containing atmosphere, and (3) arc melting of sponge of titanium plus TiN powder. Each technique produced TiN alloys containing certain amounts of oxygen carried with the constituent raw materials. Reference 9 contains more details on the processes used to manufacture these specimens. Figure 3 shows the specimens as they were received and before any further processing. When first manufactured, these specimens were cut into nominally 3-inch-diameter disks. These TiN synthetic specimens were considered as a good simulation of a hard alpha inclusion from a properties point of view and were intended to be used for measuring the three nonlinear coefficients of interest in this program, namely, TEC, ATC, and AEC. The specimens were cut into uniform parallelepiped specimens of dimensions 0.22 by 0.38 by 1.0 inch and had 2.5%, 3.1%, 3.8%, 4.8%, and 5.9% nitrogen percentage by weight. Figure 4 shows these specimens after cutting, along with the proper percent nitrogen content by weight. Note the evident porosity of the specimens at higher levels of nitrogen content (4.8% and 5.9%).

FIGURE 3. SYNTHETIC TiN SPECIMENS AS RECEIVED AND BEFORE CUTTING

FIGURE 4. SYNTHETIC TiN SPECIMENS AFTER CUTTING INTO 0.22- BY 0.38- BY 1.0-inch PARALLELEPIPED SPECIMENS

In addition to the above specimens and to allow comparative measurements of the three nonlinear coefficient of the synthetic TiN specimens to those measured on the host materials Ti-6Al-4V for contrast assessment, similar 0.22- by 0.38- by 1.0-inch parallelepiped specimens were prepared from billet and forging Ti-6Al-4V specimens. These specimens are shown in figure 5.

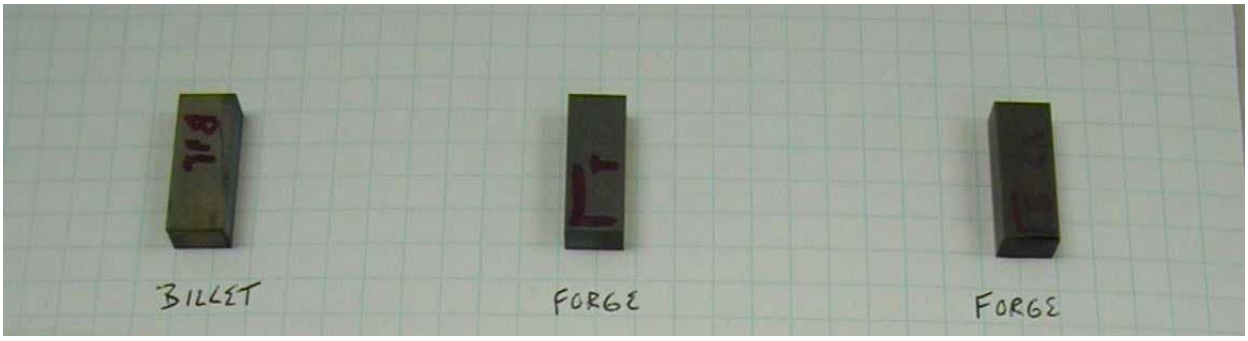

FIGURE 5. BILLET AND FORGING Ti-6Al-4V SPECIMENS AFTER CUTTING INTO 0.22- BY 0.38- BY 1.0-inch PARALLELEPIPED SPECIMENS

2.2 SYNTHETIC INCLUSIONS (TiN) EMBEDDED IN Ti-6Al-4V BLOCK.

A Ti-6Al-4V specimen with three synthetic cylindrical inclusions, manufactured using one of the methods indicated in section 2.1, was obtained from the NDE branch at WPAFB in Dayton, OH. This block was originally manufactured by GE GRC by cutting out TiN cylindrical pieces from disks similar to those shown in figure 3. Two blocks of Ti-6Al-4V with approximate dimensions of 1.0 by 2.0 by 3.0 inches and 0.5 by 2.0 by 3.0 inches were used. In the two blocks, three different but matching cylindrical cavities of the same size as the cylindrical inclusions were machined. The inclusions were inserted in them in such a way that two of the cylindrical inclusions were inserted with their axes perpendicular to the surface of the block, and the third was inserted with its axis parallel to the surface. Note that the inclusions were inserted in such a way that half of the inclusion lies in each of the two blocks. The second block was then placed on top of the first one, and they were diffusion-bonded together. Figure 6 shows the final specimen, along with the overall dimensions.

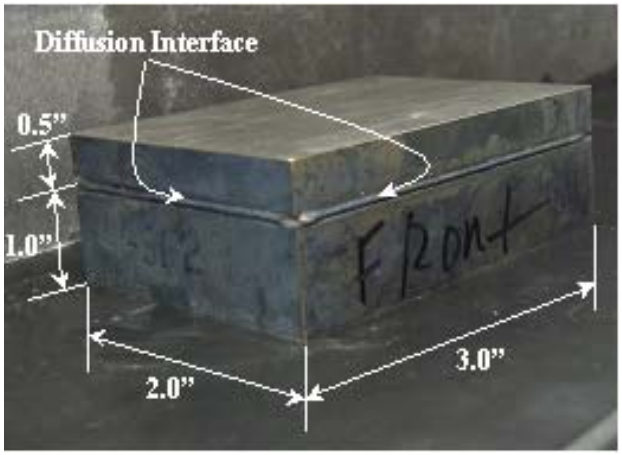

FIGURE 6. Ti-6Al-4V SPECIMEN WITH THREE CYLINDRICAL SYNTHETIC TiN INCLUSIONS

This block was intended for use in the technique validation experiments with the assumption that the inserted inclusions are representative of the condition of an unvoided hard alpha inclusion in Ti-6Al-4V. After the initial inspection of the block, using backscattered UT inspection, it became very evident that this artificial inclusion specimen was not representative of the case of unvoided hard alpha inclusions in titanium alloys. Figure 7 shows the peak reflected amplitude C-scan images of the Ti-6Al-4V specimen with synthetic cylindrical inclusions for the cases of the UT transducer focused at the (a) the diffusion bond line and (b) at the tip of the cylinders with axes perpendicular to the diffusion bond line. The measurements were done using a Sonix Acoustic Microscope Quantum 350 with a 15-MHz, 0.5-inch-diameter Panametrics V319 (serial number 326433) spherically focused UT transducer. It is very clear from the figure that the inclusions are very much detectable. As a matter of fact, the response from the inclusions perpendicular to the bond line saturated the instrumentation. This clearly shows that this specimen was not representative of the case of unvoided hard alpha inclusion in titanium alloys, as such defects are extremely difficult to detect using backscattered UT inspection.

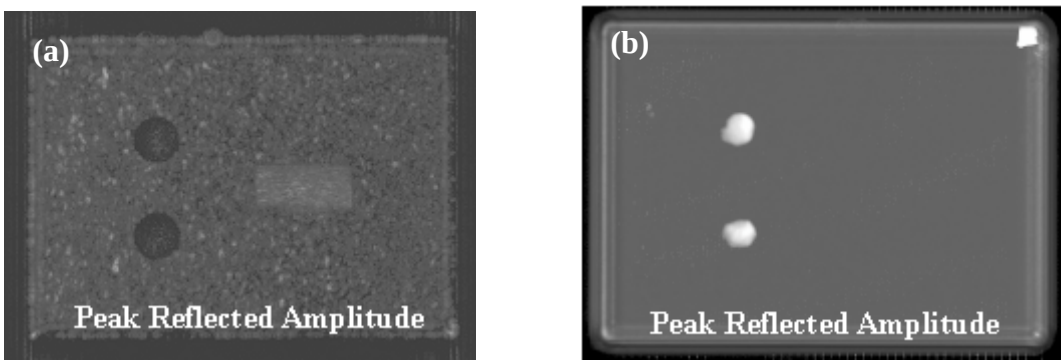

FIGURE 7. PEAK REFLECTED AMPLITUDE C-SCAN IMAGES OF THE Ti-6Al-4V WITH SYNTHETIC CYLINDRICAL INCLUSIONS WITH THE UT TRANSDUCER FOCUSED AT (a) THE DIFFUSION BOND LINE AND (b) THE TIP OF THE CYLINDERS WITH AXES PERPENDICULAR TO THE DIFFUSION BOND LINE

Several factors can account for the very strong response received from these inclusions. First, the interface between the inclusions and the titanium host materials is sharp in terms of the change in nitrogen content, which is not the case for a naturally occurring hard alpha inclusion. Second, the porosity associated with such inclusions (specially the ones with the high nitrogen content) may contribute to a higher that expected UT signal. And finally, the questionable diffusion interface between the inclusion and the host material may result in such a high signal if the inclusion is not completely bonded to the host material. For all these reasons, this specimen was deemed to be not representative of naturally occurring hard alpha inclusions in titanium alloys, and therefore, was not used in any further activities in this program.

2.3 NATURALLY OCCURRING VOIDED HARD ALPHA INCLUSIONS.

In February 1995, the FAA-funded programs, the Engine Titanium Consortium and Turbine Rotor Materials Design program, were made aware of the existence of a contaminated heat of Ti-6Al-4V. The contaminated heat, number 883588-02, occurred as the result of loss of power during melting. Following completion of the double VAR processing, the ingot was split in two and converted to the final billet diameter of 6 inches. Note that this is not the standard practice for rotor-grade materials, which are typically either triple VAR or cold hearth melting/VAR processed and rotary forged from ingot to final billet geometry. However, the original customer did not intend to use the material for aerospace applications, hence, the difference in processing. The supplier indicated that this heat was formulated from 72% revert, 28% sponge, and was chamber welded. The primary ingot was piggy-back melted; the first electrode was melted uneventfully. Partway into the second melt, a total melt shop power outage occurred. The power outage shut down the vacuum pumps, and a pressure spike occurred before the furnace was back filled with argon. After power returned, melting was resumed to complete the primary ingot. The primary ingot was inverted and remelted to complete the processing. The initial inspection of the heat was completed using conventional 5-MHz transducers in two wave modes, longitudinal and refracted shear, which led to the detection of multiple indications. Based on the UT results, the heat was dispositioned for further commercial use. Further inspection of the heat using an MZI system revealed even more indications that were not detected by conventional inspection. To ensure that the defect types were typical of hard alpha defects found in

rotor-quality materials, an assessment was made with input from the ETC and TRMD teams along with representatives from the metallurgy staff at the OEMs. Based on the chemical analysis and metallographic sectioning of the initial defects, it was determined that these defects were representative and, therefore, appropriate for further study. To ensure the appropriateness of the material for further study in that program, chemical and metallographic analyses were performed on two of the indications. The bulk composition consisted of C-0.02, N-0.014, Fe-0.18, Al-5.56, V-4.10, O-0.18, and Y-<50 parts per million, within the range of typical Ti-6Al-4V. The purpose of the study was to characterize the inclusion as a typical hard alpha inclusion, compared to inclusions previously removed from billet products or from forged components. As reported by Bogan [5], the inclusion was a hard, brittle, cracked, and voided hard alpha, containing up to 12.6% nitrogen and surrounded by diffusion zone, and could be considered typical of those encountered in billet and forged products. Microprobe data showed that the highest nitrogen areas contained approximately 1.5%-2.0% vanadium with approximately 0.1%-0.9% aluminum (Al). For more details on the CBS, see reference 6.

For the purposes of this program, several billet pieces having about 15 indications left over from the CBS were obtained from the ETC team. A number of these indications were verified again in these billets using the MZI procedure, and their locations in the respective billets were pinpointed. In particular, a 25.75-inch-long billet section (B2W2C) containing two indications, X and D, was extensively studied. After precisely locating the two defects in the billet, they were cut out from the billet material to form two blocks with dimensions of 2 by 2 by 2.82 inches and 2 by 2.73 by 2.82 inches, respectively. Figure 8 illustrates the location of the two indications in the original billet. Figure 9 shows the two blocks, each containing one indication after they were cut out from the billet.

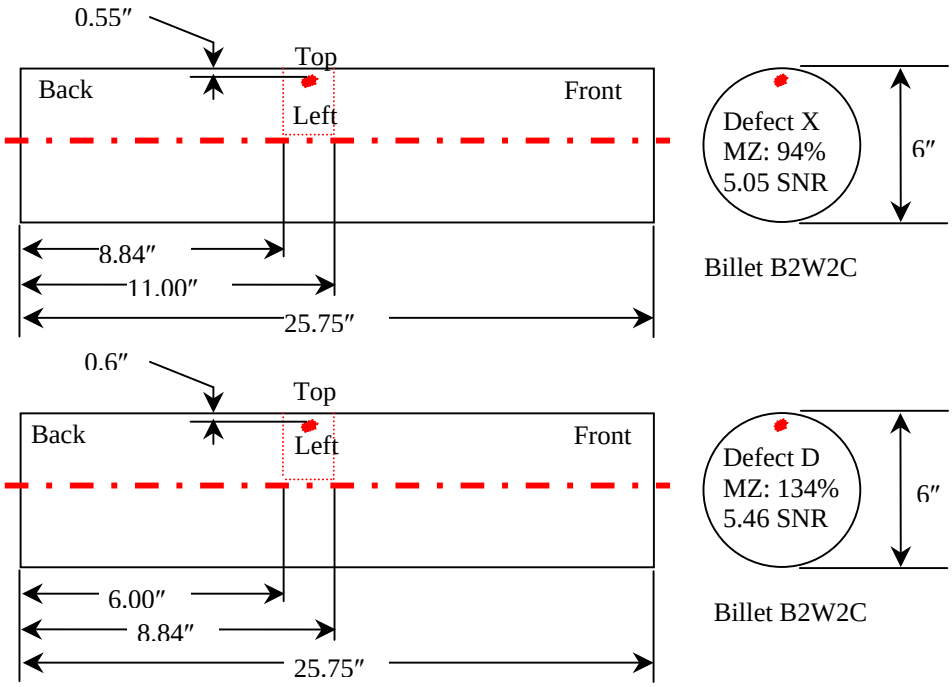

FIGURE 8. LOCATIONS OF DEFECTS X AND D IN BILLET B2W2C

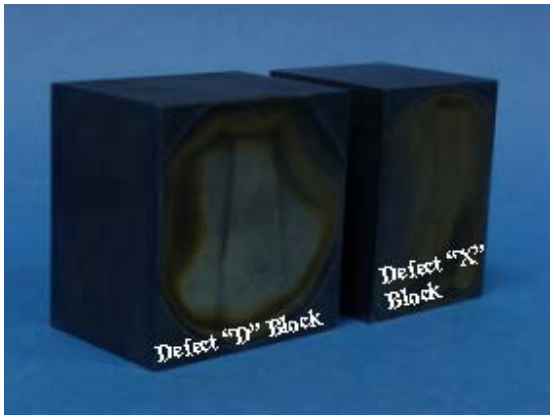

FIGURE 9. TWO BLOCKS CONTAINING DEFECTS X AND D

To verify that the defects are still in the blocks, the two blocks were ultrasonically inspected using a 5.5-MHz, 0.75-inch-diameter, spherically focused transducer with a 6-inch focal length. A 6-inch water path was used so that the transducer could be focused on the front wall of the block facing the transducer. Figure 10 shows C-scan images of defect X as obtained from characterizing the defect in the block from six different directions. The defect dimensions are estimated from the C-scans to be 0.625 inch in length, 0.230 inch in height, and 0.100 inch in thickness. Time-of-flight (TOF) measurements verifying the presence of the defect are shown in figure 11. Similar data is shown in figures 12 and 13 for defect D. In this case, the inclusion is estimated to be 1.19 inches in length, 0.270 inch in height, and 0.100 inch in thickness, based on the C-scan images. It is worth mentioning here that the UT response obtained from these two inclusions is largely attributed to the voids associated with the inclusions and the acoustic impedance contrast between these voids and the titanium host material.

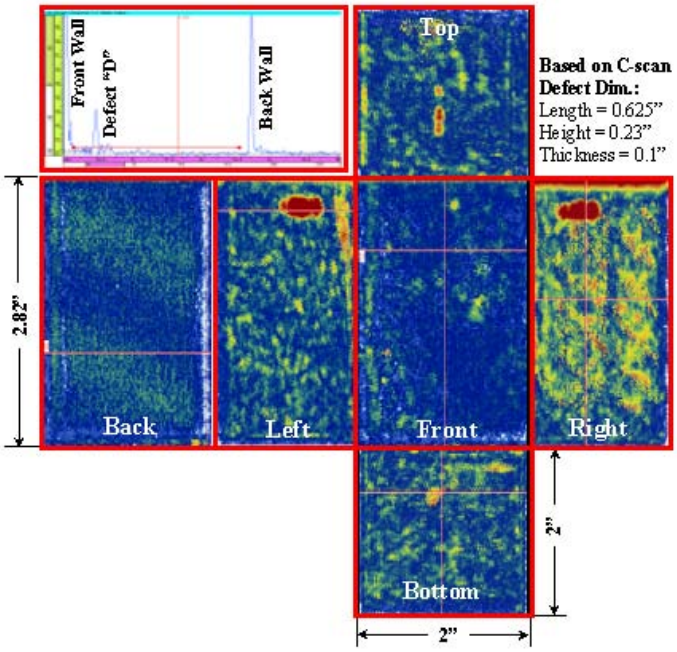

FIGURE 10. C-SCAN IMAGES OF DEFECT X

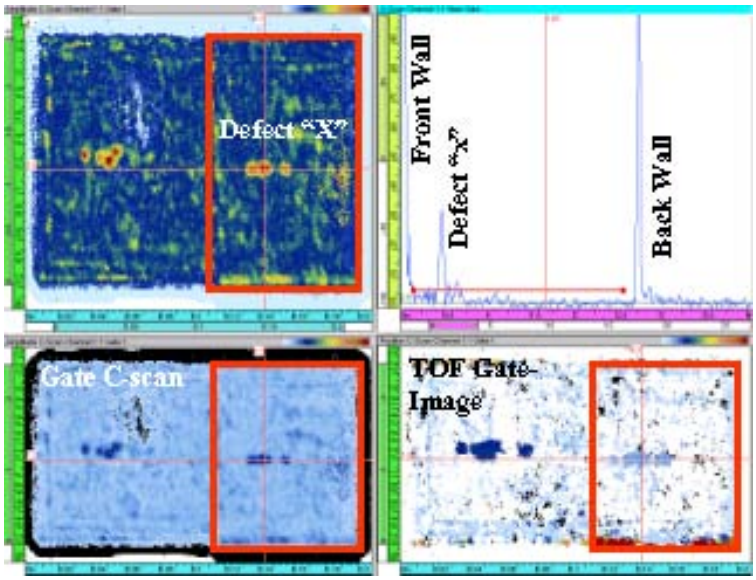

FIGURE 11. TIME OF FLIGHT DATA FOR DEFECT X

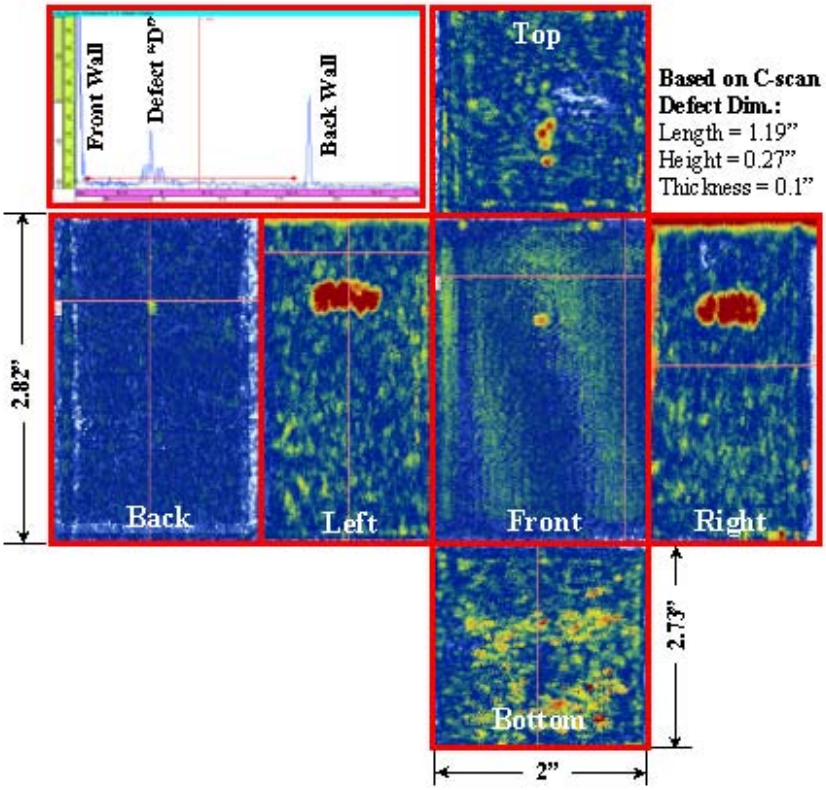

FIGURE 12. C-SCAN IMAGES OF DEFECT D

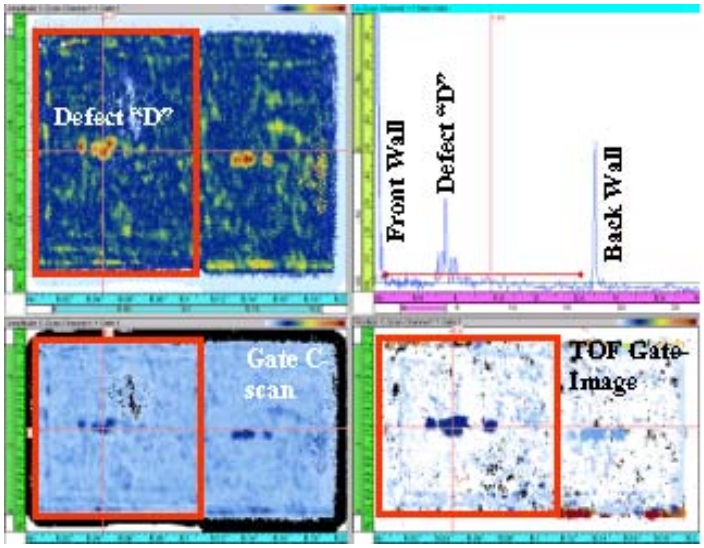

FIGURE 13. TIME OF FLIGHT DATA FOR DEFECT D

These two defects were HIPped to heal at 1650°F and 30 ksi pressure for 5 hours with the intention of creating samples representative of unvoided hard alpha inclusions to be used in the technique validation experiments. After the HIPping process was completed, the two blocks were re-inspected using the same procedure described above and no indication of the two defects were observed in both the backscattered C-scan images or the TOF images. Figures 14 and 15 show the results for defect X after HIPping. Figures 16 and 17 show similar results for defect D.

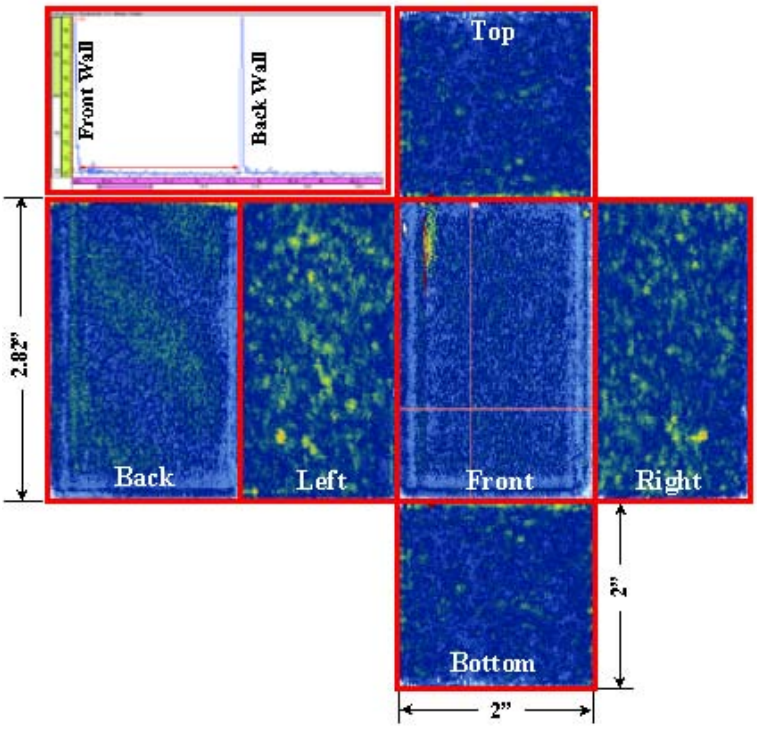

FIGURE 14. C-SCAN IMAGES OF THE BLOCK CONTAINING DEFECT X

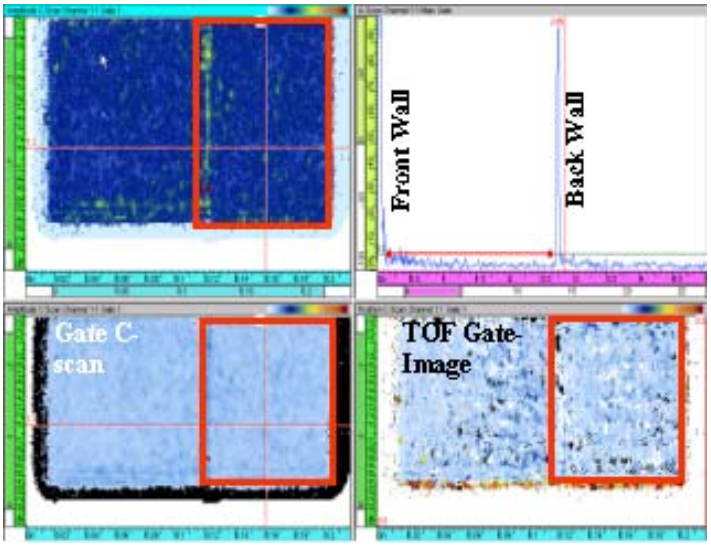

FIGURE 15. TIME OF FLIGHT DATA FOR THE BLOCK CONTAINING DEFECT X

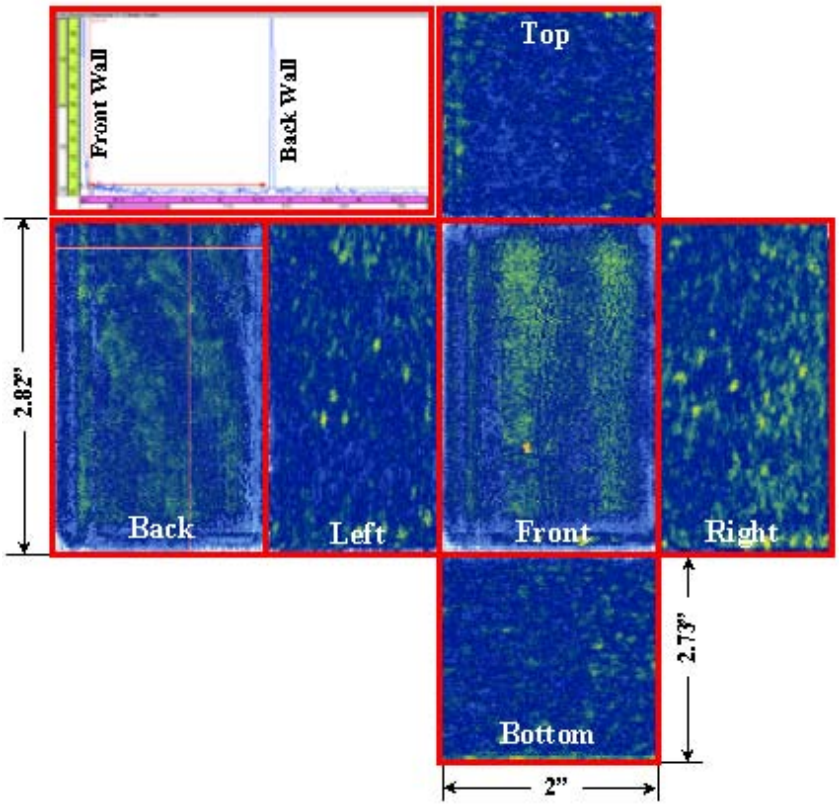

FIGURE 16. C-SCAN IMAGES OF THE BLOCK CONTAINING DEFECT D

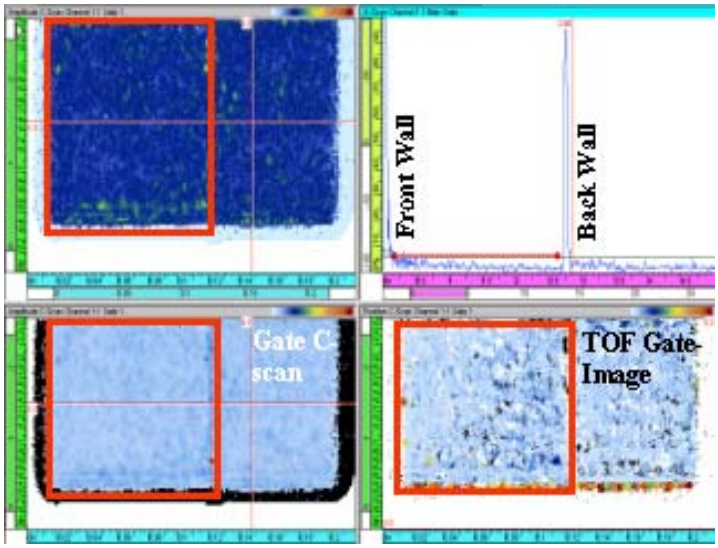

FIGURE 17. TIME OF FLIGHT DATA FOR THE BLOCK CONTAINING DEFECT D

3. EXPERIMENTAL SETUP FOR MEASUREMENT OF THE THREE NONLINEAR PARAMETERS.

3.1 THERMAL EXPANSION COEFFICIENT MEASUREMENTS.

A schematic diagram and the experimental setup of the thermal expansion measurement are shown in figures 18 and 19, respectively. The thermal expansion tests were done on an Orton Dilatometer Model 1600D. A dilatometer measures the percent linear change (PLC) in a specimen as it is heated by means of a linear variable differential transducer (LVDT). Put simply, the LVDT is an alternating current device with a magnet and two coils that can very accurately measure displacement. The thermal extension of the specimen can be measured since the LVDT is connected to a spring-loaded pushrod that rests against the specimen. The spring compresses as the specimen expands, and this displacement is monitored by the LVDT. A furnace encircles the specimen and can be heated up to 1600°C in this particular model. A reference specimen made of alumina and a reference file was provided with the dilatometer equipment. A calibration run with the alumina specimen was made initially and compared with the reference values given by Orton so that the accuracy of the dilatometer could be ensured. The calibration runs closely matched the reference plot provided by the vendor, but it was not exactly the same; therefore, it was corrected so that future runs could be more accurate. Once the calibration run was completed, a calibration file was created with the necessary corrections and was used for all subsequent runs with other materials.

The software accompanying the dilatometer made the experimental measurements relatively easy. The program included a simple sheet with boxes clearly labeled to enter the specimen length, create a heating program, enter a file to save data, and specify which calibration file will be used. All runs started at room temperature and were heated at 3°C/minute to 500°C. Nominally, the specimen length was 1 inch. Once an experimental run was started, a graph showed the PLC versus temperature and the data was written to a user-created file. The information could then be imported into an spreadsheet for further analysis, namely, to calculate

the differential coefficient of expansion (DCE) and the average coefficient of expansion (ACE), which is the value given in most textbooks.

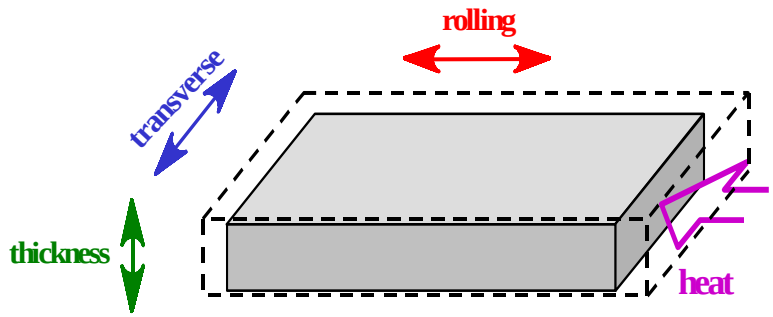

FIGURE 18. SCHEMATIC DIAGRAM OF THE TEC MEASUREMENTS

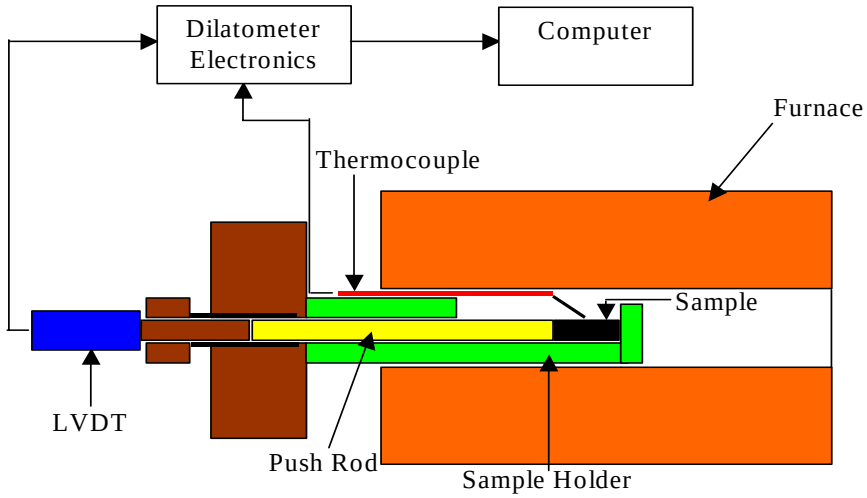

FIGURE 19. EXPERIMENTAL SETUP FOR TEC MEASUREMENTS

3.2 ACOUSTOELASTIC COEFFICIENT MEASUREMENTS.

The goal of acoustoelastic measurements is to measure the relative velocity versus stress in a specimen. Figure 20 shows a schematic diagram of the direction of loading from the material test system (MTS) and the position of the transducer for longitudinal and shear measurements, with the experimental setup of the acoustoelastic measurement shown in figure 21. This was a very difficult measurement and required some sophisticated instrumentation, namely, a Stanford Research Systems, Inc. (SRS) Universal Time Interval Counter and an SRS Four-Channel Digital Delay/Pulse Generator, a Panametrics Pulser/Receiver, and a LeCroy Waverunner digital oscilloscope. The basic concept of this measurement is straightforward. First, a signal is created on the oscilloscope by means of the Pulser/Receiver and an appropriate transducer and couplant. For longitudinal measurements, a 0.25 inch-diameter, 5-MHz transducer was used with either grease or Vaseline as the couplant, and for shear measurements, a 0.25 inch-diameter, 5-MHz transducer was used with honey as the couplant. Then, with the Digital Delay/Pulse Generator,

an arming gate is placed around the first two echoes from the specimen. This arm specifies the region in which the time interval counter (TIC) measures the time delay. For accurate time measurement, one must choose to measure the corresponding positive or negative zero crossings on the first and second back-wall echoes of the specimen. It is important to choose common points on each pulse to obtain an accurate reading. The MTS program, through input channel 1, reads the time delay from the digital-to-analog (D/A) output marked MEAN on the TIC instrument. The apparent velocity can be determined directly from the measured propagation time delay and the nominal thickness of the specimen. To determine the actual sound velocity, the thickness of the specimen must be corrected for changes due to the Poisson effect.

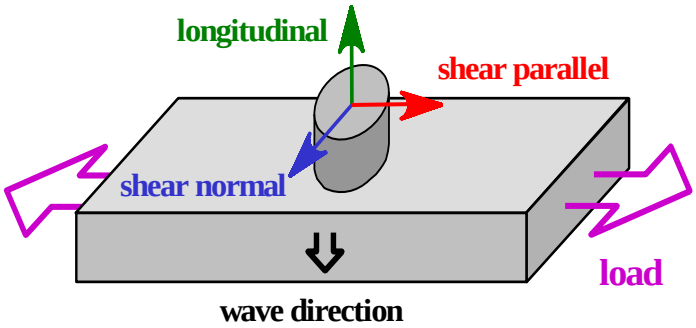

FIGURE 20. SCHEMATIC DIAGRAM OF THE AEC MEASUREMENTS

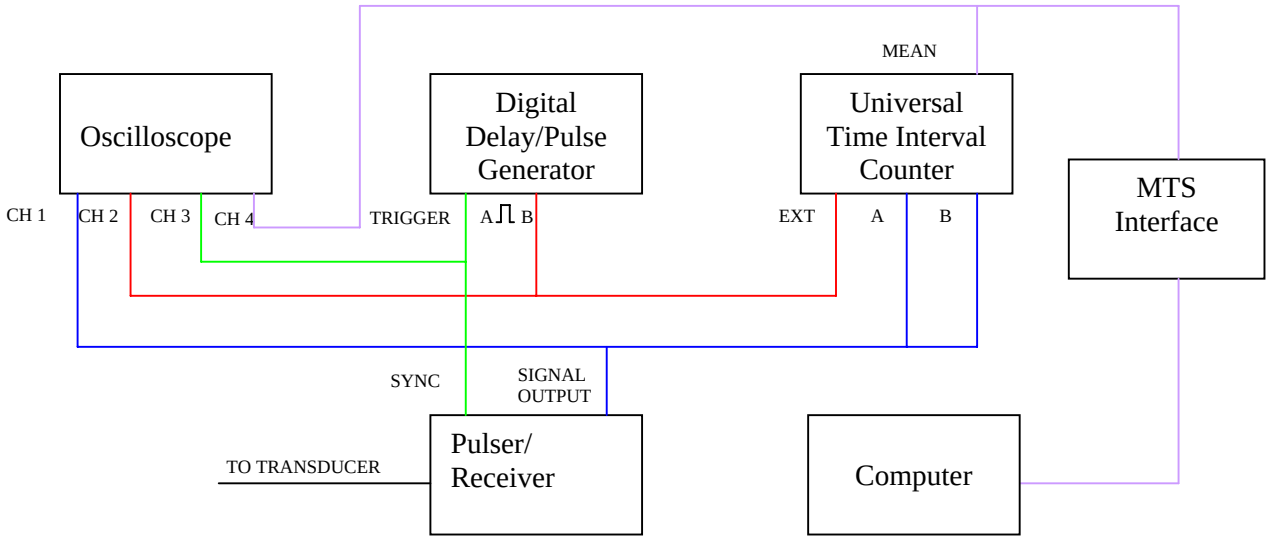

FIGURE 21. EXPERIMENTAL SETUP FOR AEC MEASUREMENTS

Once a good signal was established, the specimen was placed in the MTS and set in place. This meant gripping both ends of the specimen while the transducer was clamped somewhere in the middle of the specimen. A simple program was created on the MTS software for the acoustoelastic measurements. This program dwells for 2 seconds, then cycles at 0.05 Hz for 30 cycles at a stress level of 1/3 the nominal yield stress of the material. During the experiment, the axial force and the two-way propagation time delay from the TIC was plotted against time.

When the cycles were completed, the force was ramped to zero, and the program was complete. The complete data set, namely, a time stamp, the axial force from the MTS, and the two-way propagation time from the TIC, was written to a file, which could be imported into a spreadsheet for further analysis.

3.3 ACOUSTOTHERMAL COEFFICIENT MEASUREMENTS.

The goal of acoustothermal measurements is to measure the relative velocity versus temperature in a specimen. A schematic diagram and the experimental setup of the acoustothermal measurement are shown in figures 22 and 23, respectively. This is also a very complicated measurement like the acoustoelastic measurement. As can be expected, the same equipment was used to measure the time delay in the specimen, which in turn was used to calculate the velocity. However, instead of stressing the specimen in the MTS, the specimen was placed in a water bath in a Pyrex bowl and subjected to temperature variations. Five-MHz longitudinal and shear transducers were used in the acoustothermal measurements. The transducer was placed on one side of the specimen and a bracket was placed on the other side with everything clamped together and placed in the water. The bracket is U-shaped and provides a gap on the underside of the specimen where the transducer signal acts.

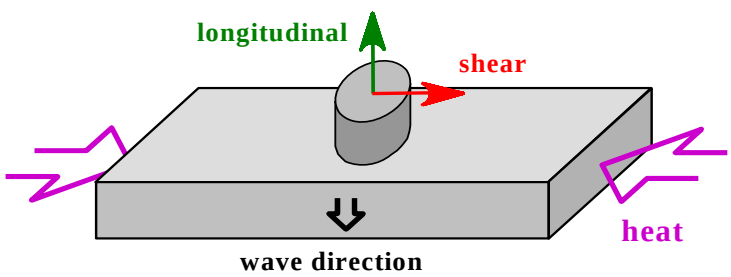

FIGURE 22. SCHEMATIC DIAGRAM OF THE ATC MEASUREMENTS

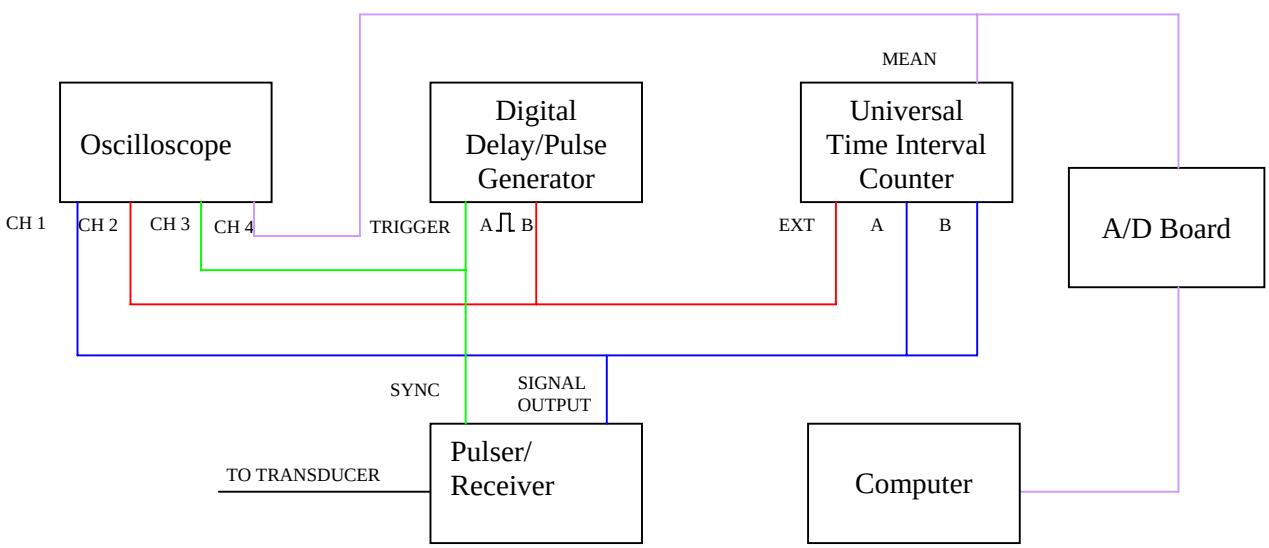

FIGURE 23. EXPERIMENTAL SETUP FOR ATC MEASUREMENTS

An identical reference specimen with a type K thermocouple mounted on it was also placed in the bath to measure the temperature. For the longitudinal measurements, the glass dish was placed on a Dataplate Digital Hot Plate to be heated. The temperature range used in these experiments was from room temperature to 80°C. The water bath was allowed to cool back to room temperature after the initial heating was finished. The cooling part of the temperature profile was slower and more reproducible; therefore, the ATC was measured in that stage. The propagation time delay increased as the temperature increased and decreased as the temperature decreased. This was recorded by a Virtual Bench Data Logger that is part of the Labview routine. A connection was made to the D/A output marked MEAN on the TIC and passed to an analog-to-digital (A/D) board. The thermocouple was also connected via a preamplifier to the A/D board to be relayed to the computer and displayed and written to a file by the Data Logger. The Data Logger displayed the temperature of the reference specimen and the two-way propagation time delay versus time. The only difference with the shear measurements was in the method of heating and cooling. The longitudinal wave couplant used was grease, and although it probably lost some of its viscosity when heated, it did not affect the measurements. Shear wave couplants lose their needed high viscosity at higher temperatures, and therefore, the signal slowly decays on the oscilloscope. Eventually, the signal disappears completely, typically around 55°-60°C. In addition to decreased viscosity, honey dissolves in water and cannot be used for the thermal measurements; therefore, a special Panametrics shear wave couplant was used in these experiments. Instead of heating on the hot plate, a Neslab chiller, which can heat and cool water, was used to extend the temperature range. The temperature was first increased from room temperature to 45°C, then cooled to 5°C. This range was broader by approximately 15°C than what would be achievable using the hot plate, since the hot plate would only allow the specimen to be heated to 45°C, then cooled to room temperature.

The effect of temperature on the strength of the UT signal in the case of shear wave UT measuremets was further investigated in a study that used different couplants. In the following sections, the results from the above measurements are presented and discussed in detail.

4. RESULTS FROM THE EXPERIMENTAL MEASUREMENTS OF THE THREE NONLINEAR PARAMETERS.

4.1 THERMAL EXPANSION COEFFICIENT.

Materials can be characterized by a TEC that measures how much the material expands over a certain temperature range. This parameter was mostly used to compare materials, referred to as ACE, but other parameters can be calculated as well, including the PLC and DCE. The ACE was of the most interest in the experiments conducted in this study. The PLC is the percentage that the specimen expanded from its original length, or

$$PLC = \frac{l_T - l_0}{l_0} \times 100 \tag{1}$$

where l_0 is the original length of the specimen, and l_T is the length of the specimen at the final temperature. The DCE is the amount the specimen expanded from its orginal length over a 20° temperature range

$$DCE = \frac{(l_T - l_{T-20})/l_0}{20} \tag{2}$$

where $l_{T\text{-}20}$ is the length at a temperature that is 20° less than the final temperature. Finally, the ACE is the amount the specimen expanded from its original length over the entire temperature range of the experiment

$$ACE = \frac{(l_T - l_0)/l_0}{T - T_0} \tag{3}$$

where T is the final temperature, and T_0 is the initial temperature. The experiments performed in this study compared pure titanium and Ti-6Al-4V titanium alloy with no nitrogen content to titanium with varying levels of nitrogen content from 2.5% to 5.9%.

Several practice runs were carried out with the dilatometer using Ti-6Al-4V specimens. The objective was to obtain results similar to the accepted TEC for this common titanium alloy, namely, $\alpha_{\text{Ti-6Al-4V}} \approx 8.6\times10^{-6}$/°C to 9.7×10^{-6}/°C between 20°C and 500°C [10]. An extensive study was done on textured Ti-6Al-4V and the results were comparable to the above values. Six specimens were machined from a large piece of forged Ti-6Al-4V. Two pieces were machined in each of the axial, transverse, and vertical directions, namely, the typical x, y, and z coordinate directions. Experimental runs were performed on these specimens, and the ACE for each orientation was calculated. The results listed in table 1 are comparable to the accepted expansion coefficient of Ti-6AL-4V, and it was determined that the dilatometer was giving accurate results.

TABLE 1. THE PLC AND ACE OF Ti-6Al-4V
DIRECTIONAL (TEXTURED) SPECIMENS

At 500°C	Axial Trial 1	Axial Trial 2	Transverse Trial 1	Transverse Trial 2	Vertical Trial 1	Vertical Trial 2
PLC (%)	0.439	0.449	0.453	0.435	0.450	0.412
ACE (10^{-6}/°C)	9.39	9.58	9.68	9.30	9.67	8.85

The next step was to test the TiN specimens provided by MLLP/Air Force Research Laboratory. These were titanium specimens of varying nitrogen content, i.e., 2.5%, 3.1%, 3.8%, 4.8%, and 5.9% nitrogen. Also provided by Honeywell Engines was a titanium billet specimen with no nitrogen content and canted and forged Ti-6Al-4V specimens. Four experimental runs were performed, and the averaged results are listed in table 1.

Figures 24 and 25 show the PLC and ACE versus temperature curves of one of the four trials. Table 2 shows that the PLC and ACE both decrease with increasing levels of nitrogen. This is to be expected since nitrogen makes titanium more brittle and brittle materials do not expand as much as the more ductile material, such as pure titanium with no nitrogen content. However, as will be shown in a following section, the relative contribution of this observed dimensional change to the overall temperature effect is very small and practically negligible.

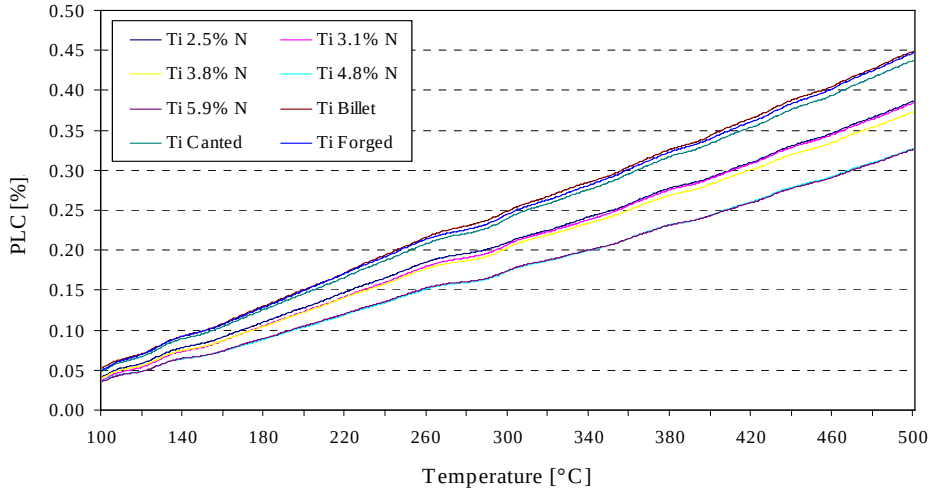

FIGURE 24. PERCENT LINEAR CHANGE VS TEMPERATURE FOR TITANIUM WITH VARYING LEVELS OF NITROGEN CONTENT

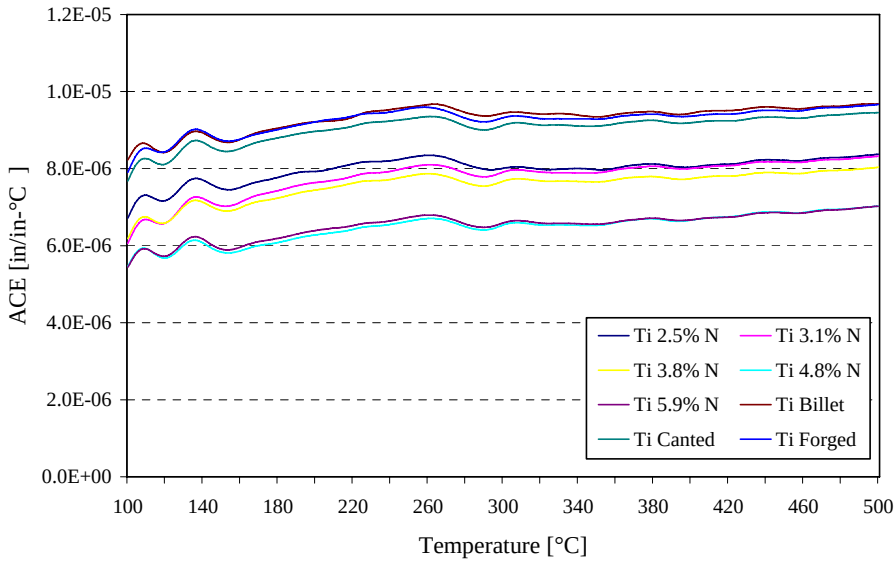

FIGURE 25. THE ACE VS TEMPERATURE FOR TITANIUM WITH VARYING LEVELS OF NITROGEN CONTENT

TABLE 2. THE PLC AND ACE OF TITANIUM SPECIMENS WITH VARYING LEVELS OF NITROGEN

At 500°C	2.5% N	3.1% N	3.8% N	4.8% N	5.9% N	Billet	Canted	Forged
PLC (%)	0.386	0.381	0.365	0.331	0.321	0.439	0.438	0.439
ACE (10^{-6}/°C)	8.29	8.19	7.81	7.08	6.88	9.41	9.39	9.41

4.2 ACOUSTOELASTIC COEFFICIENT.

The acoustoelastic measurements were the most difficult of the three measurements. Since the nitrogen-enriched specimens were very small and weakened by both embrittlement and microporosity, they could not be tested in the MTS machine for fear of breaking them. In addition, the grips of the 100-kN MTS machine could not be adapted to hold these small pieces in tension. Therefore, the specimens had to be tested in compression with a high risk of buckling failure. Also, since the variations in the acoustoelastic effect were expected to play a minimal role in the detectability of hard alpha inclusions, only baseline measurements were made in Ti-6Al-4V reference specimens without jeopardizing the small, embrittled TiN specimens.

First, a piece of Al-2024 was tested since the AEC was previously measured for this material [11]. Then a rolled piece of Ti-6Al-4V was tested in the same manner. The goal was to gather some baseline data on the AECs and to estimate the order of magnitude of the maximum relative change in velocity that could be seen in the presence of thermal stresses. Both longitudinal and shear transducers were used in these measurements. Data acquisition was controlled by the MTS program. A shear transducer was also used at normal and parallel polarization, meaning the particle displacements were aligned normal and parallel to the direction of the unidirectional stress, respectively. The crucial part of the measurements was to measure the relative change of the instantaneous time delay by the TIC. The initial time delay was recorded before the MTS program was started, and then the Set Rel(ative) button on the TIC was pressed so that the measurements would be taken relative to this initial time delay. The MTS data acquisition system also recorded the voltages at the initial time delay and when it was zeroed at the start of the measurement for subsequent calibration of the analog output signal of the TIC. The time, applied force, and analog output from the TIC were written to a file as the program was executed.

Also very important for the measurement was the scaling factor on the TIC. The scaling factor is a measure of how much the input signal to the computer, i.e., the analog output of the TIC, changes for a given change in time delay. The scaling factor had to be adjusted on a case-by-case basis to avoid saturating the output signal from the TIC. The available signal is from 0-8 V and the scaling factor was increased for shear measurements since the relative increase in the time delay was greater than in the longitudinal measurements. For Al-2024, the scaling factor was set to 5,000 for longitudinal measurements and 10,000 for shear measurements. For Ti-6Al-4V, the scaling factor was set to 2000 for longitudinal measurements and 5000 for shear measurements.

Once the data was imported into Excel, the relative velocity was calculated. From the time delays that were recorded before the program started, relative change in the two-way propagation time $\Delta t / t_0$ was calculated from

$$\frac{\Delta t}{t_0} = \frac{A(V - V_0)}{t_0} \tag{4}$$

where A [μs/V] is the measured slope associated with the scaling factor, V [V] is the analog output of the TIC recorded by the computer as the specimen is stressed and written to file, V_0 [V]

is the analog output of the TIC recorded once the Set Rel button was pressed, and t_0 [μs] is the initial time delay recorded by the operator from the TIC.

The measured slope value is dependent on the scaling factor. It was calculated by first obtaining a signal on the oscilloscope with a transducer using a generic specimen, then pressing the Set Rel button. The relative value on the TIC and the corresponding voltage on the MTS were then recorded several times. Next, the transducer was moved to a different spot on the specimen, where the thickness was, inevitably, slightly different, and the procedure was repeated. In this way, a well-controlled time delay could be simulated for calibration purposes. The averaged time delays at both transducer locations from the TIC were then subtracted. The same procedure was followed for the average values of the voltages recorded by the A/D converter. The results were finally divided to obtain a slope in μs/V. In this way; the entire data acquisition system could be accurately calibrated without calibrating each element of the system separately.

The Poisson correction was then made to account for the changing cross-sectional area as the specimen was put in tension and compression. The lateral strain is given by

$$\frac{\Delta d}{d_0} = -\frac{\sigma \nu}{E} \tag{5}$$

where σ is the applied stress, ν is Poisson's ratio in the material, and E is the modulus of elasticity. For Al-2024, σ was varied from -15 to 15 ksi with a corresponding cross-sectional area of S = 0.5 in^2, ν = 0.33, and E = 10,700 ksi. For Ti-6Al-4V, σ was varied from -30 to 30 ksi with a corresponding cross-sectional area of S = 0.203 in^2, ν = 0.33, and E = 16,500 ksi. Without the Poisson correction, the slope of the relative velocity versus stress curve is larger than with the correction since some of the apparent velocity change is due to the Poisson effect. Using the correction yields a more accurate AEC. Finally, the relative velocity change is the Poisson correction minus $\Delta t / t_0$, or

$$\left.\frac{\Delta c}{c_0}\right|_{\mathrm{AE}} = -\frac{\sigma \nu}{E} - \frac{\Delta t}{t_0} \tag{6}$$

Figures 26 and 27 show typical examples of the relative velocity versus stress in Al-2024 using a 0.25-inch-diameter, 5-MHz longitudinal transducer and a 0.25-inch-diameter, 5-MHz shear transducer at both normal and parallel polarizations. The slope of the graph of the relative velocity versus stress is the AEC, K. The corresponding AECs, using a straight-line approximation, are 6.2×10^{-5}, 6.4×10^{-5}, and -15.3×10^{-5} ksi^{-1} for longitudinal and shear waves at normal and parallel polarizations, respectively. These values are in reasonable agreement with a previously published report [10].

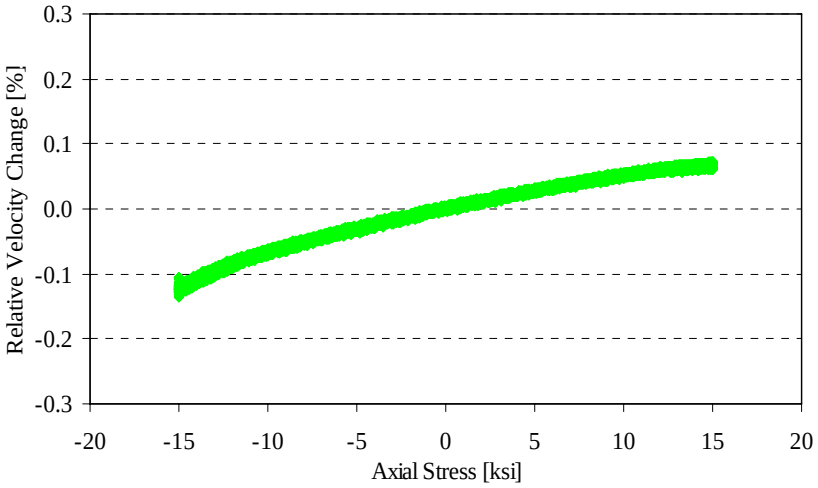

FIGURE 26. RELATIVE VELOCITY CHANGE VS STRESS IN Al-2024 USING A LONGITUDINAL TRANSDUCER

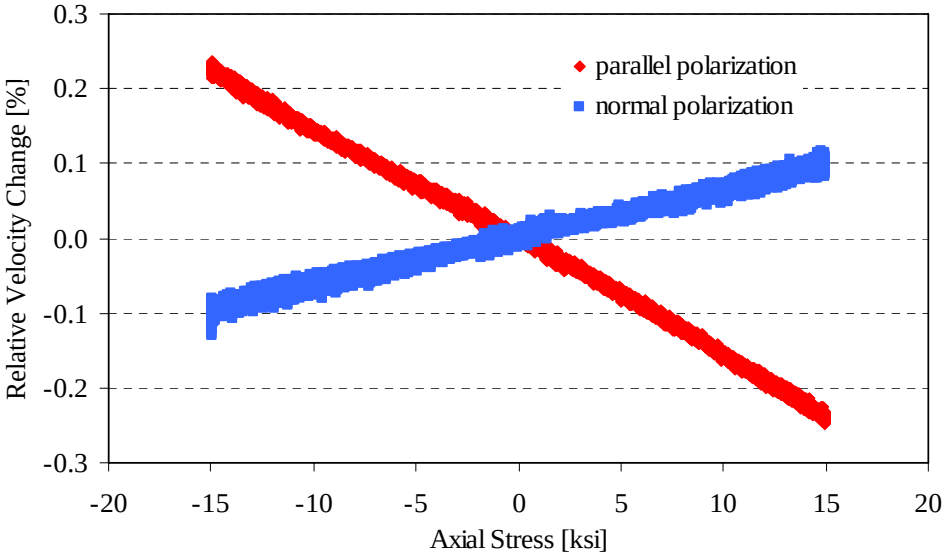

FIGURE 27. RELATIVE VELOCITY CHANGE VS STRESS IN Al-2024 USING A SHEAR TRANSDUCER

Similarly, figures 28 and 29 show typical examples of the relative velocity versus stress in Ti-6Al-4V using a 0.25-inch-diameter, 5-MHz longitudinal transducer and a 0.25-inch-diameter, 5-MHz shear transducer at normal and parallel polarizations. The corresponding AECs, using a straight-line approximation, are 1.4×10^{-5}, 7×10^{-5}, and -11.5×10^{-5} ksi^{-1} for longitudinal and shear waves at normal and parallel polarization, respectively.

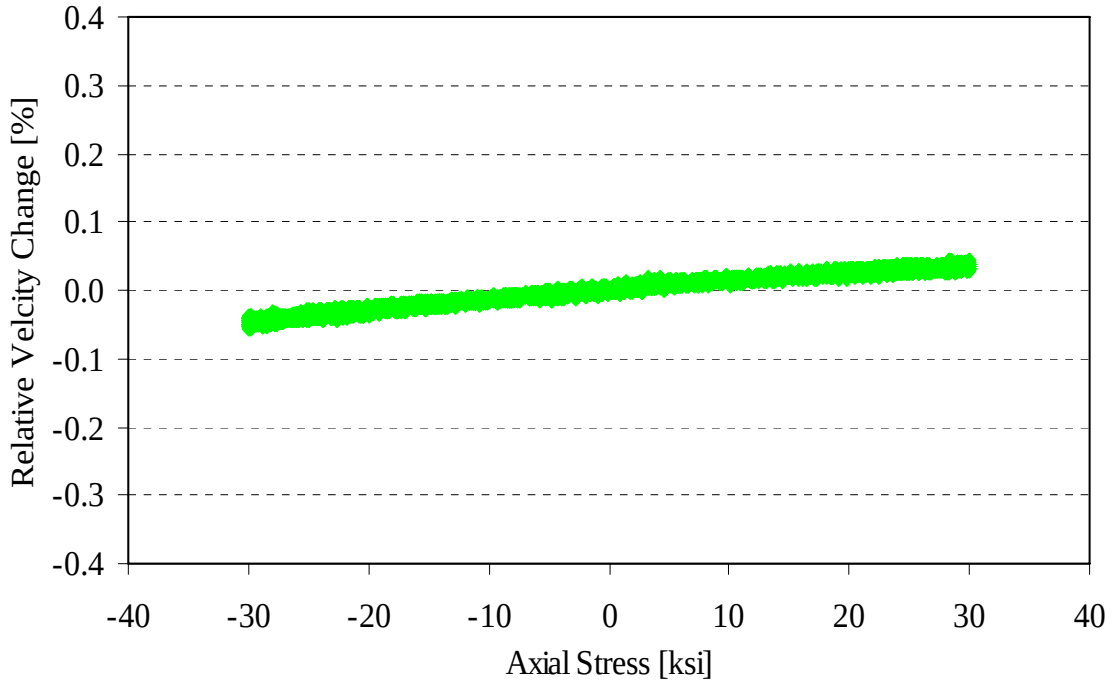

FIGURE 28. RELATIVE VELOCITY CHANGE VS STRESS IN Ti-6Al-4V USING A LONGITUDINAL TRANSDUCER

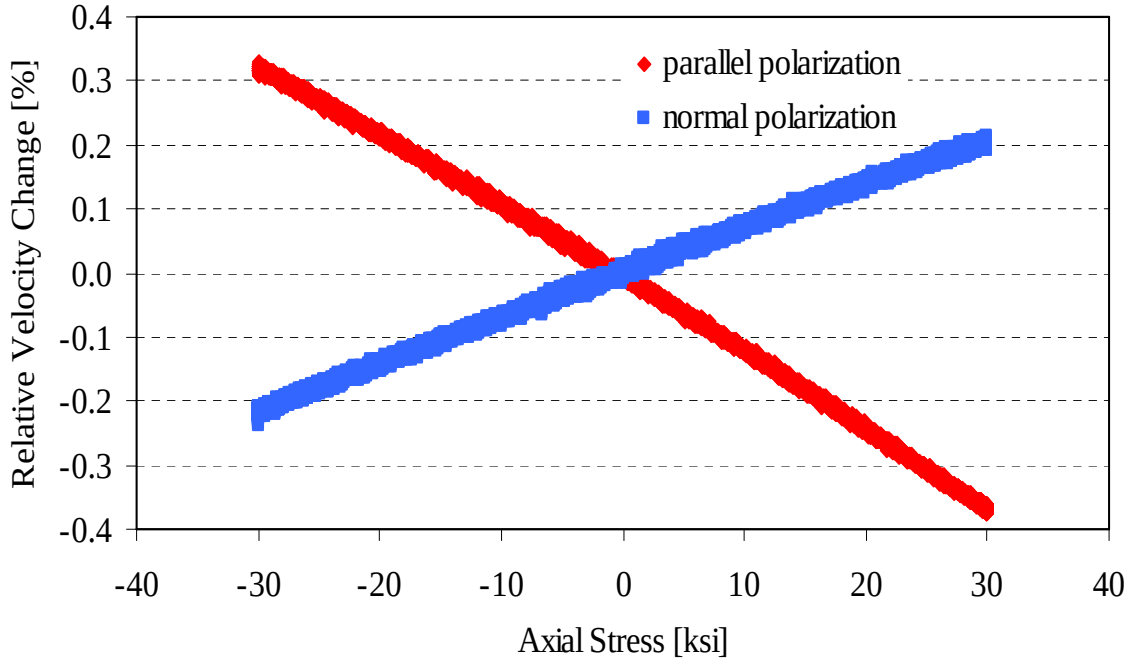

FIGURE 29. RELATIVE VELOCITY CHANGE VS STRESS IN Ti-6Al-4V USING A SHEAR TRANSDUCER

As can be seen, the AECs are very small because the relative velocity changes merely 1% at stress levels as high as the yield strength of the material. It would be possible to test the effect of nitrogen in titanium with either larger specimens or at lower levels of applied stress, but the evaluation of the data would be susceptible to large errors because of the small change in relative velocity. Using a larger stress range would be dangerous, too, because there would be a risk of breaking the specimens.

4.3 ACOUSTOTHERMAL COEFFICIENT.

The acoustothermal measurement was very similar to the acoustoelastic measurement in that the same equipment is used to measure the time delay. The calculation of the relative velocity was somewhat simpler than discussed above because, for simplicity, only the apparent velocity was analyzed without correcting for the changing propagation length due to thermal expansion, i.e., the apparent velocity change includes a small part due to changes in dimension. Once the data was imported into Excel from the Data Logger, the apparent relative velocity change was calculated from

$$\frac{\Delta c_{apparent}}{c_0} = -\frac{\Delta t}{t_0} = -\frac{A\Delta V}{t_0} \tag{7}$$

where, as before, A [μs/V] is the measured slope associated with the scaling factor, ΔV [V] is the change in the analog output signal from the TIC, and t_0 [μs] is the initial time delay recorded by the operator on the TIC.

Among the specimens that were tested, titanium grade 2 and rolled Ti-6Al-4V were included. These specimens were only tested for a better comparison in addition to the specimens described previously. Each specimen had an identical counterpart to be used as the reference for temperature measurements so that electrical grounding problems could be avoided. The specimens provided by Honeywell Engines, namely, a forged Ti-6Al-4V specimen and a titanium billet specimen, as well as the 2.5% N, 3.1% N, and 3.8% N titanium specimens from AFRL, were also tested in the same way. The Ti-6Al-4V-canted specimen was used as the reference specimen when these specimens were tested. The goal was to obtain six acceptable velocity versus temperature plots for each specimen, using both longitudinal and shear wave transducers. To limit gross measurement errors, acceptable experimental data was defined as a curve with a linear regression of R^2 = 0.95 or better. This acoustothermal test was a very complicated one, and it became excessively difficult with the smaller specimens. Many factors can easily hinder the experiment, such as the amount of couplant on the transducer, the water level in the bath, or even a degenerating (thermally aging) transducer. Therefore, the R^2 criterion was imposed to accept only sufficiently linear velocity versus temperature curves. Tables 3 and 4 list the averaged ATCs of the tested specimens and the corresponding standard deviations for longitudinal and shear waves, respectively.

TABLE 3. MEASURED AVERAGED ATCs USING A 5-MHz LONGITUDINAL TRANSDUCER

	ATC (10^{-4}/°C)						
	Titanium	Ti-6Al-4V	Forged	Billet	2.5% N	3.1% N	3.8% N
Average	-2.41	-2.35	-2.10	-1.92	-2.32	-1.86	-1.20
Std. Dev.	0.10	0.28	0.19	0.47	0.25	0.42	0.16

TABLE 4. MEASURED AVERAGED ATCs USING A 5-MHz SHEAR TRANSDUCER

	ATC (10^{-4}/°C)						
	Titanium	Ti-6Al-4V	Forged	Billet	2.5% N	3.1% N	3.8% N
Average	-6.86	-8.94	-7.28	-7.65	-6.96	-8.01	-12.86
Std. Dev.	0.44	0.61	0.28	0.33	0.57	0.48	0.48

To illustrate the actual raw data used to obtain the results listed in tables 3 and 4, figures 30 and 31 show two measured velocity versus temperature graphs for the 3.1% TiN specimen. Figure 30 shows an acceptable curve of R^2 = 0.996, whereas figure 31 shows a curve of R^2 = 0.919 that was determined to be unacceptable because of its excessive nonlinearity.

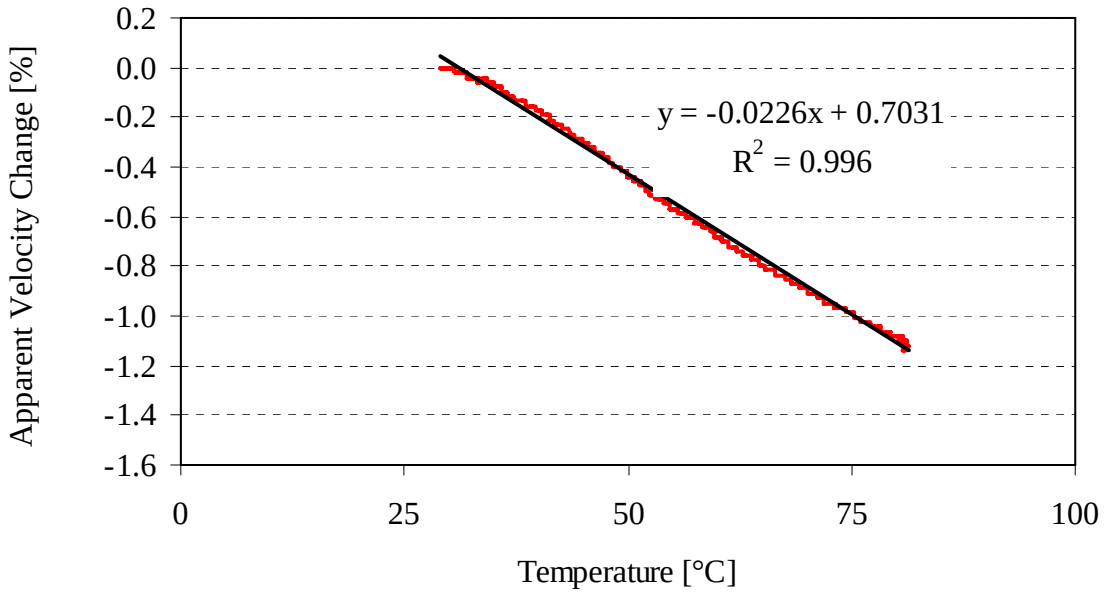

FIGURE 30. APPARENT VELOCITY CHANGE VS TEMPERATURE IN TITANIUM WITH 3.1% N USING A LONGITUDINAL TRANSDUCER (ACCEPTABLE DATA)

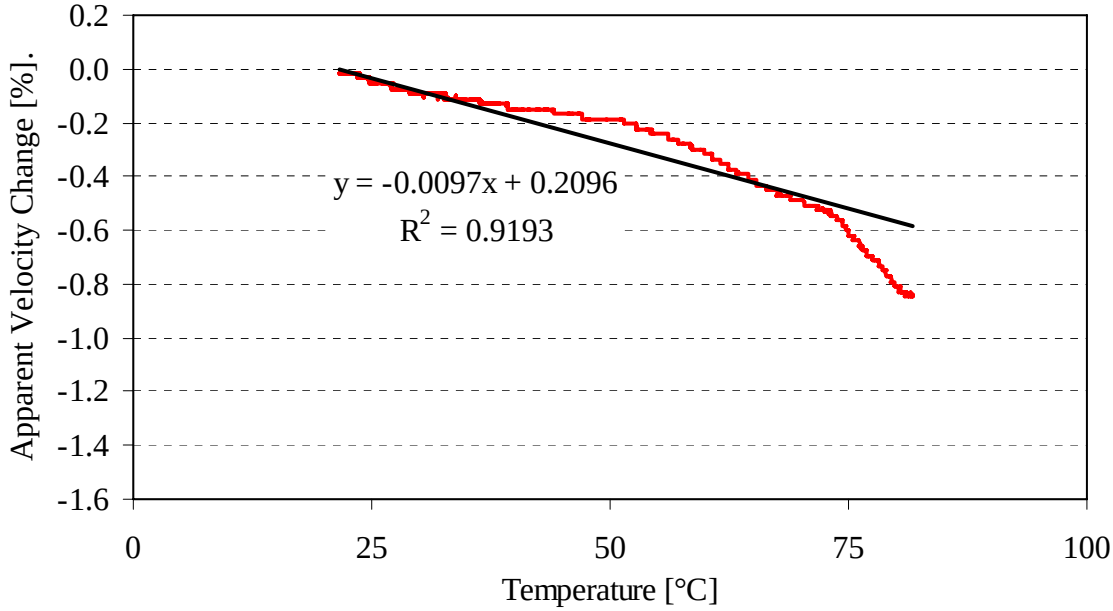

FIGURE 31. APPARENT VELOCITY CHANGE VS TEMPERATURE IN TITANIUM WITH 3.1% N USING A LONGITUDINAL TRANSDUCER (UNACCEPTABLE DATA)

Even without positively identifying the underlying physical mechanism or mechanisms responsible for the observed variation in the ATC, the reliability and accuracy of the results could be increased by eliminating the obvious artifacts of excessively low coefficient of determination ($R^2 < 0.95$). Figure 32 shows the distribution of the coefficient of determination versus the longitudinal ATC (β) after filtering. Even the filtered data exhibits an obvious trend of decreasing coefficient of determination, i.e., lower level of confidence in the accuracy and reliability of the data, with decreasing magnitude of the ATC. Unfortunately, increasing the threshold R^2 value used for filtering would eliminate most of the data on the difficult to measure TiN specimens of high nitrogen content; therefore, further experiments will be needed to increase the accuracy of these results. Figure 33 shows a graphical representation of the crucial data listed in table 3. The error bars indicate the full range of the measured values. It should be noted that the apparent decrease in variation shown for the 3.8% TiN specimen is due to the small number of successful runs (only three) rather than to good reproducibility. Actually, the fairly strong, implicit correlation illustrated in figure 32 (between the increasing nitrogen content and decreasing measurement) repeatability suggests that the dominating uncertainty is somehow related to the reduced consistency (microporosity, microcracks, inhomogeneous grain structure, etc.) of the TiN specimens. Therefore, additional measurements should be taken on the TiN specimens to further investigate the possibility of increasing the measurement accuracy on these specimens by better controlling the transducer and couplant parameters and by improving data acquisition.

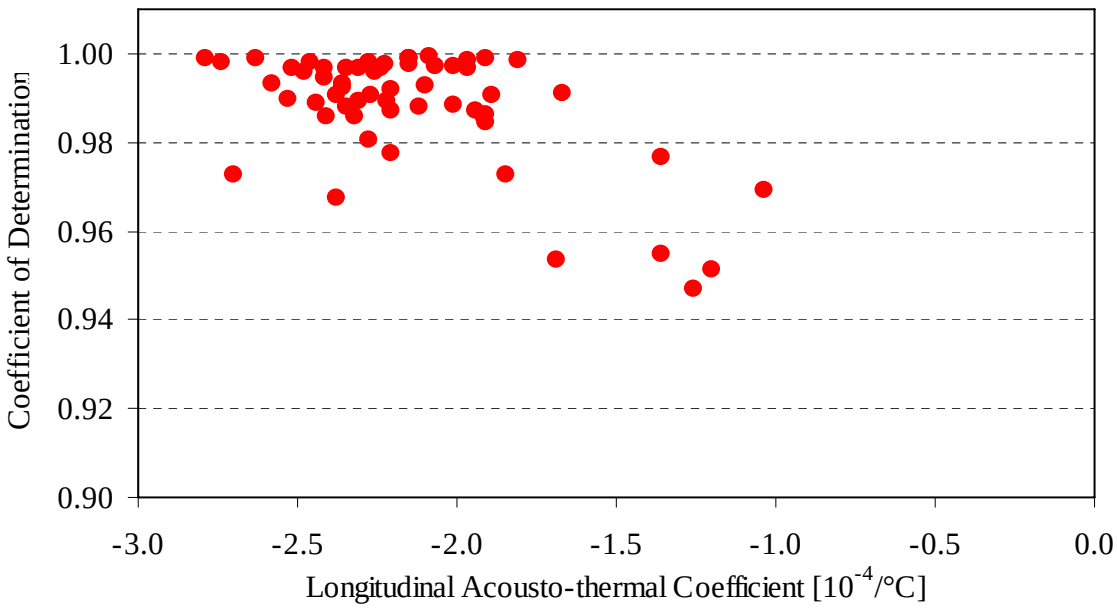

FIGURE 32. DISTRIBUTION OF THE COEFFICIENT OF DETERMINATION (R^2) VS THE LONGITUDINAL ATC (β)

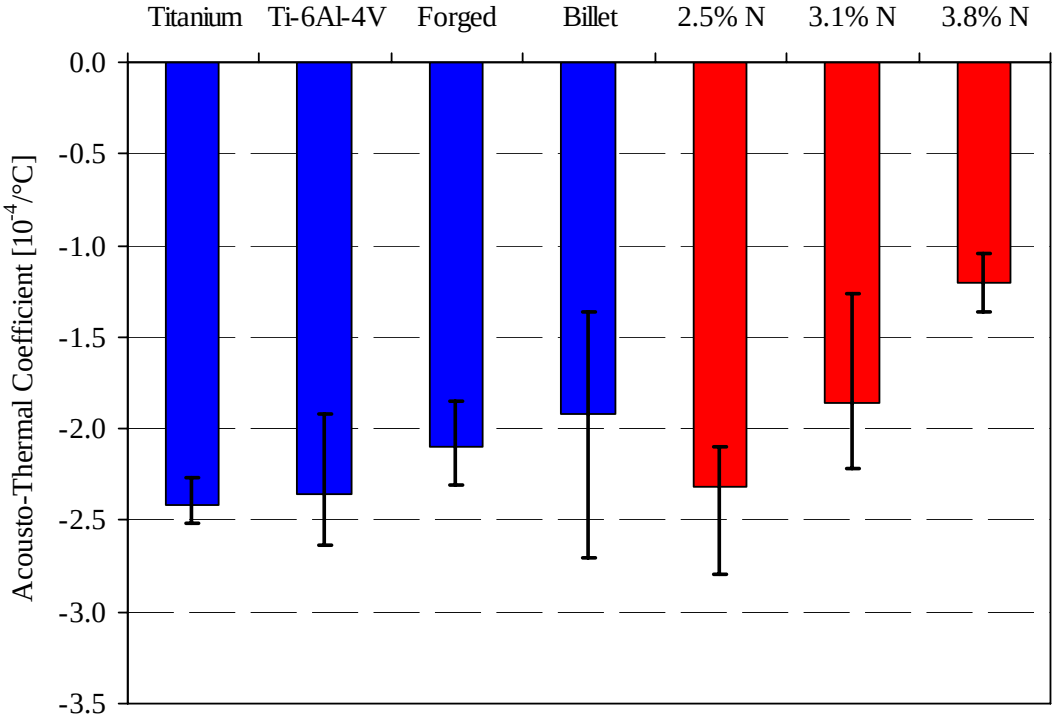

FIGURE 33. REPRESENTATION OF THE LONGITUDINAL ATC DATA LISTED IN TABLE 3

5. RELATIVE CONTRIBUTIONS TO THE OVERALL THERMAL EFFECT.

Three factors contribute to the changing propagation time when a specimen is heated, i.e., the geometrical change due to thermal expansion (α), the acoustoelastic contribution (K), and the acoustothermal contribution (β). The relative velocity change caused by each contribution can be expressed by the following formula

$$\frac{\Delta c}{c_0} = \frac{\Delta d}{d_0} - \frac{\Delta t}{t_0} \tag{8}$$

where t is the time of arrival of the sound wave, d is the distance that the wave travels, and c is the speed of the sound. By means of a simple example, it can be determined which mechanism produces the dominating effect that should be examined further. A TiN specimen of 4%-6% nitrogen content and a temperature change of $\Delta T = 50°C$ is assumed in the following example.

The dimensional change due to unrestrained thermal expansion can be expressed as

$$\left.\frac{\Delta d}{d_0}\right|_{\mathrm{TE}} = \alpha \Delta T \tag{9}$$

where the TECs of Ti-6Al-4V and Ti-3.8%N are known from the experiments done previously, $\alpha_{\text{Ti-6Al-4V}} \approx 10\times10^{-6}/°C$ and $\alpha_{\text{TiN}} \approx 7\times10^{-6}/°C$ (with a slight overestimation of the difference to be conservative). Therefore, the expected maximum differential strain due to thermal expansion can be calculated as follows:

$$\varepsilon_{\max} = \frac{\Delta d_{\text{Ti-6Al-4V}} - \Delta d_{\text{TiN}}}{d_0} \approx (\alpha_{\text{Ti-6Al-4V}} - \alpha_{\text{TiN}})\Delta T = 1.5\times10^{-4} \tag{10}$$

The corresponding maximum thermal stress can be expressed as

$$\sigma_{\max} = E\,\varepsilon_{\max} \approx 2.5\,\text{ksi} \tag{11}$$

where $E = 1.65\times10^4$ ksi is the known modulus of elasticity in Ti-6Al-4V [10]. The acoustoelastic contribution can be expressed as follows:

$$\left.\frac{\Delta c}{c_0}\right|_{\mathrm{AE}} = K\sigma \tag{12}$$

where $K \approx 6\times10^{-5}$ ksi^{-1} denotes the magnitude of the average expected AEC of Ti-6Al-4V so that the estimated upper limit for the resulting velocity change is

$$\left.\frac{\Delta c}{c_0}\right|_{\mathrm{AE}} \approx K\sigma_{\max} = 1.5\times10^{-4} \tag{13}$$

which is the same as the value of the maximum differential thermal strain from equation 10.

The acoustothermal contribution can be expressed as follows

$$\left.\frac{\Delta c}{c_0}\right|_{\mathrm{AT}} = \beta \Delta T \tag{14}$$

Because of the relatively low level of thermal expansion, equation 14 can be approximated by

$$\left.\frac{\Delta c}{c_0}\right|_{\mathrm{AT}} \approx -\left.\frac{\Delta t}{t_0}\right|_{\mathrm{AT}} = \beta_a \Delta T \approx 0.65\% \tag{15}$$

where β_a is the measured apparent ATC without correction for thermal expansion which is a much weaker effect (for Ti-6Al-4 $\beta_a \approx -2.3\times10^{-4}$/°C and -8.9×10^{-4}/°C for longitudinal and shear waves, respectively, versus $\alpha \approx 1\times10^{-5}$/°C).

Since the thermally induced acoustoelastic effect was found to cause only a minor relative velocity change of $\approx 3\times10^{-6}$ for 1ºC (33.8ºF) change in temperature (see equation 13 for 50ºC (122ºF)), it was concluded that the dominating effect is that of the thermal modulation of sound velocity, i.e., the ATC, and that the other contributions, namely, the thermal expansion and the acoustoelastic effects, are essentially negligible. This is the reason why the ATC is emphasized in the rest of this report and the other two contributions are assumed to be negligible.

6. VELOCITY MEASUREMENTS.

The longitudinal and shear velocities were measured in the titanium grade 2, Ti-6Al-4V rolled, forged, and canted specimens, the titanium billet, as well as the 2.5% N, 3.1% N, and 3.8% N titanium specimens. The setup was used because it accurately measures the absolute propagation time delay in the specimen. From this, the unperturbed velocity c_0 is easily calculated as

$$c_0 = \frac{2\,d_0}{t_0} \tag{16}$$

where d_0 is the unperturbed thickness of the specimen measured by calipers, and t_0 is the unperturbed two-way propagation delay measured by the Time Interval Counter. Figures 34 and 35 show that, as expected, the sound velocity in TiN increases by roughly 3% with each weight percent of nitrogen, which is in good agreement with the findings from previous studies [12].

The specimens with 4.8% N and 5.9% N were not measured since no detectable signal could be obtained. These specimens were too porous and neither a longitudinal nor a shear wave could propagate all the way through them and back. Thus, they could not be used in the acoustothermal measurements either.

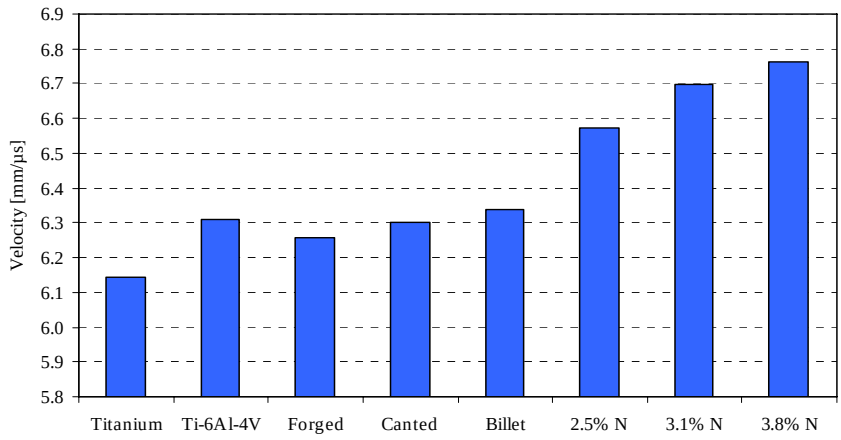

FIGURE 34. LONGITUDINAL VELOCITY IN TITANIUM WITH VARYING LEVELS OF N CONTENT

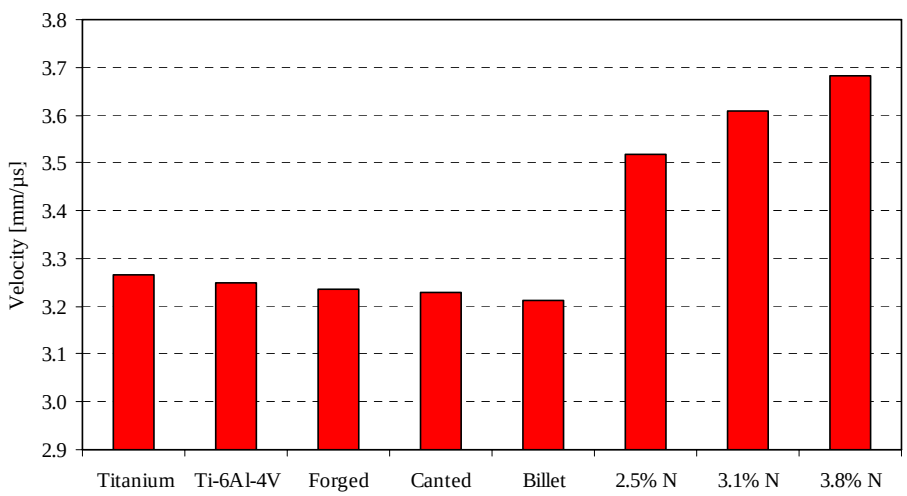

FIGURE 35. SHEAR VELOCITY IN TITANIUM WITH VARYING LEVELS OF N CONTENT

7. NUMERICAL SIMULATION FOR PRELIMINARY FEASIBLITY ASSESSEMENT.

From the results presented previously (see equation 15), it was concluded that the acoustothermal effect is the dominant effect amongst the three measured nonlinear parameters. For a 50°C change in temperature, it was predicted that there would be approximately 0.65% change in velocity, which is less than the previously estimated upper limit of 1.0% velocity change. To assess the possibility of measuring any phase modulations of a propagating longitudinal wave due to such small velocity change, the UT finite difference-wave propagation simulation software, Wave2000Pro, was used in various simulations. Figure 36 shows the basic setup used in the simulations. A rectangular 60- x 50-mm piece of Ti-6Al-4V was used to simulate the host material. The acoustic properties of Ti-6Al-4V were taken as density $\rho = 4500$ kg/m^3, longitudinal sound speed $c_L = 6070$ m/sec, and shear sound speed $c_s = 3310$ m/sec. Embedded

in the titanium alloy was a cigar-shaped inclusion with certain dimensions. Based on previous studies (see reference 6) and earlier C-scan images (see figure 10), it was estimated that an inclusion representing defect X would be 15 mm long and 4 mm wide. These dimensions were used in the first model investigated. The green regions in figure 36 represent infinite boundary conditions to eliminate or minimize any reflections from these edges of the finite model.

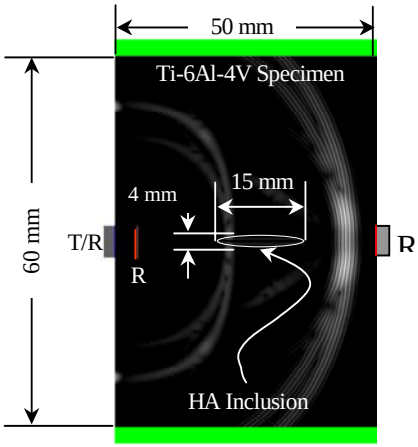

FIGURE 36. A NUMERICAL SIMULATION MODEL SETUP

Figure 37 shows the results corresponding to this simulation model. Several scenarios were investigated with the longitudinal-wave velocity in the inclusion modulated up to 6% from that of the host alloy. Figure 37(a) shows the results corresponding to the case of a 5-MHz, 10-mm-diameter transmitter and a 10-mm-diameter receiver in pulse-echo configuration. Figure 37(b) shows similar results for the case of a 5-MHz, 10-mm-diameter transmitter and a 1-mm-diameter receiver in a pitch-catch configuration. Figure 37(c) shows similar results for the case of 5-MHz, 10-mm-diameter transmitter, 10-mm-diameter receiver again in a pitch-catch configuration. Careful inspection of these figures show that the peak of the received signal starts to shift to the left (arrives earlier due to higher speed) up to about 4% velocity modulations. Beyond that, an interference phenomenon takes over and shifts the peak to the right, implying lower phase modulation compared to the host material. Figure 38 shows a plot of the absolute time shift in the peak of the signal in nanoseconds (nsec) versus the sound speed modulation in percent for the three scenarios depicted in figure 37. Note that in figure 38, the time shift for the pulse-echo case was divided by two to reflect the fact that the sound makes a two-way round trip before arriving at the receiver and to facilitate the comparison with the pitch catch case. It is also noted that for the case of the 1-mm-diameter receiver, the time shift in the peak is much higher as the sound speed modulation is increased compared to the other two cases due to the much higher spatial resolution of the wave front that reduces the averaging of the phase front compared to the 10-mm-diameter receiver. Since the acoustothermal modulation of the sound speed, as measured experimentally, is approximately 0.65%. A peak shift of about 11 nsec was expected, which can be easily measured in a laboratory environment. This is, off course, subject to the validity of the assumption, which includes (1) the size of the defect used in the simulations is appropriate, (2) the sound velocity in TiN increases by roughly 3% with each weight percent of nitrogen, and (3) the shape of the inclusion used in the simulations, is reflective of the actual defects.

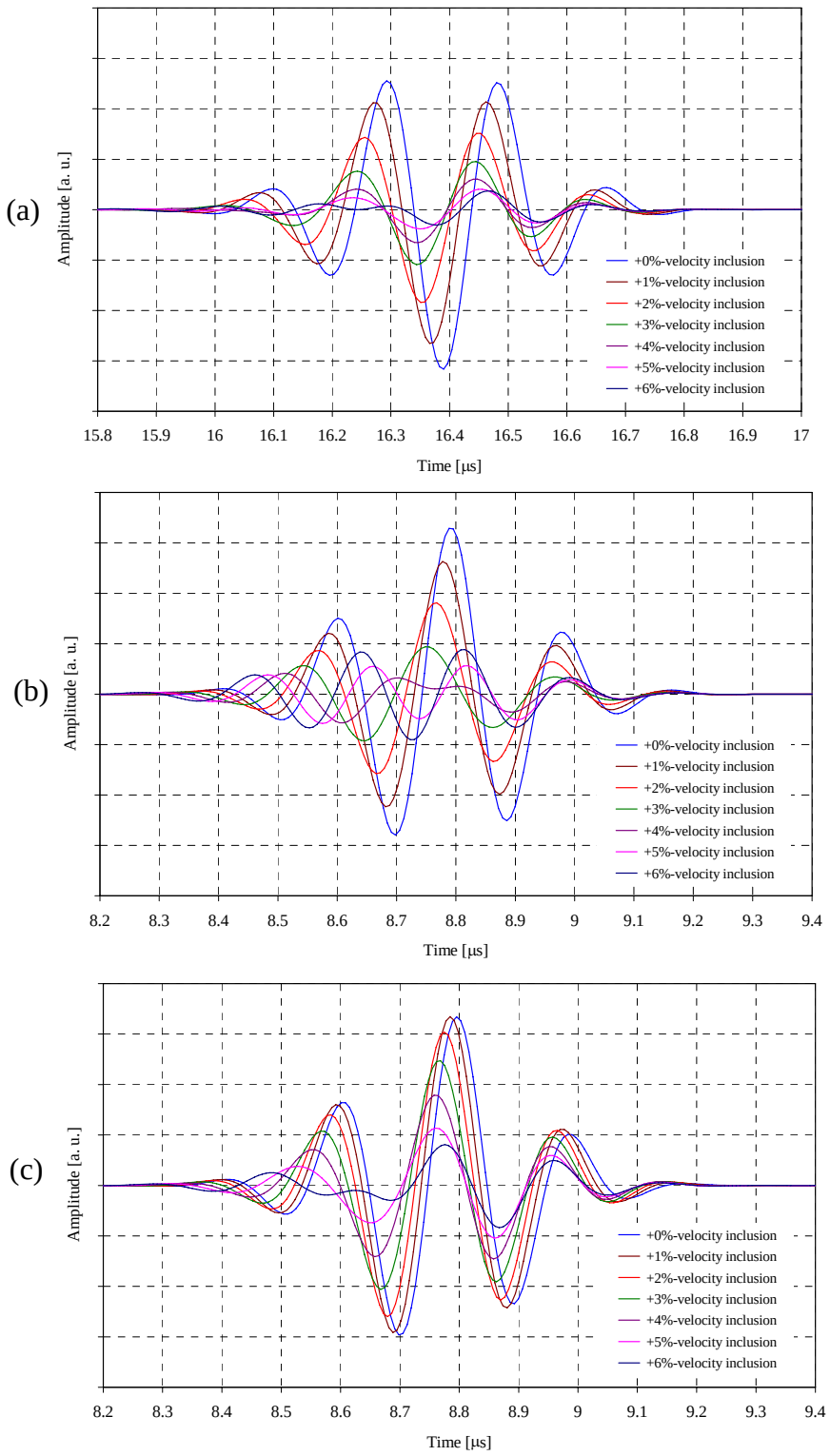

FIGURE 37. SIMULATION RESULTS FOR A CIGAR-SHAPED INCLUSION 15 mm LONG AND 4 mm WIDE

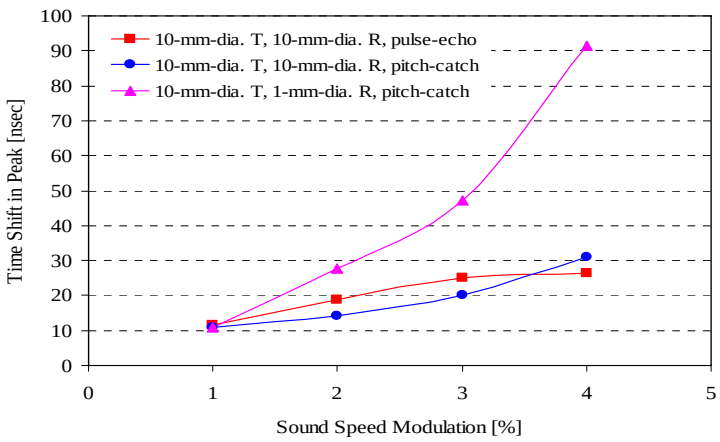

FIGURE 38. ANALYSIS OF THE TIME SHIFT IN THE PEAK DUE TO SOUND SPEED MODULATION IN THE INCLUSION FOR THE SCENARIOS DEPICTED IN FIGURE 37

The above results suggest that one should be able to detect the presence of defects X and D after HIPping at least in the scan representing the TOF data. Referring back to figures 15 and 16, one sees that there is no indication of the defects in any of the scans obtained. This implies that one of the assumptions used in the simulation models must be invalid. To verify previous results on defect X and to understand which of the assumptions could be questionable, the block with defect X was rescanned using the Sonix Quantum–350 acoustic microscope and a higher frequency 10-MHz, 0.5-inch-diameter Panametrics V311 UT transducer. The data acquired were the peak and TOF of the back-wall reflected signal. Figure 39 shows these results and again confirms that no indication of the presence of defect X was observed. Since the other two assumptions were fairly verified in this and other studies, it seems that the assumption on the size of the defect is the one most questionable. Figure 40 shows the results of similar simulations as those presented in figure 37 with the 15-mm-long and 4-mm-wide inclusion replaced by a 15-mm-long by 1-mm-wide inclusion. A quick analysis of figure 40 reveals that the time shift of the signal peak for the later case is much smaller and suggests that the assumed defect size is probably inaccurate. This promoted further investigation of defect X by performing a metallurgical analysis and using other NDE techniques as detailed in the next section.

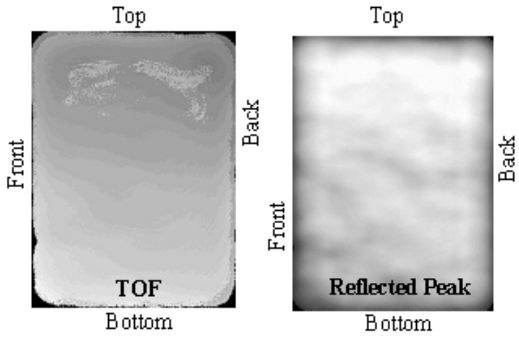

FIGURE 39. THE TOF AND REFLECTED PEAK AMPLITUDE SCANS FOR DEFECT X

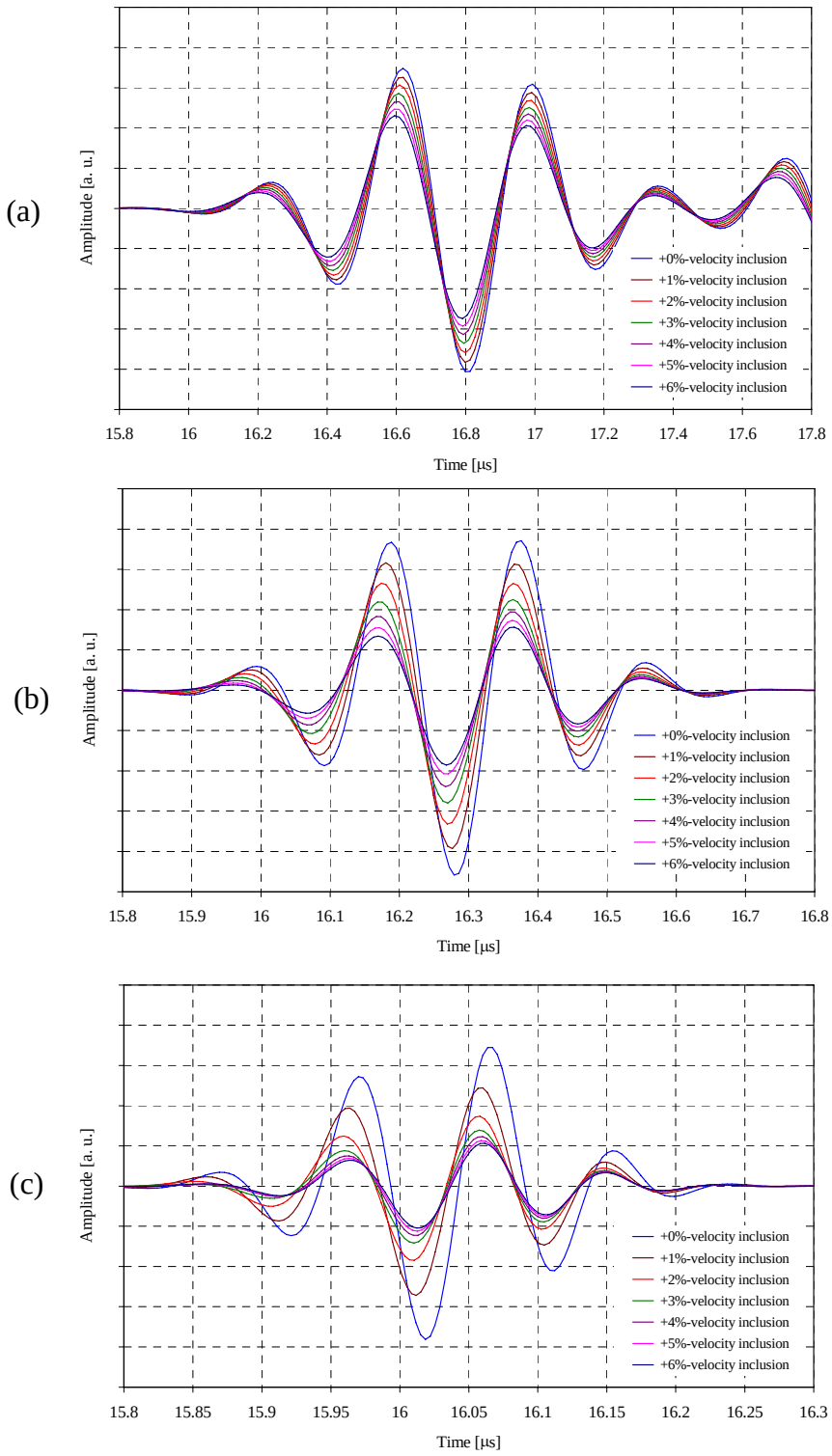

FIGURE 40. SIMULATION RESULTS FOR A CIGAR-SHAPED INCLUSION 15 mm LONG AND 1 mm WIDE

8. FURTHER ANALYSIS OF DEFECT X.

8.1 EDDY-CURRENT AND ACOUSTIC MICROSCOPY IMAGING.

To further characterize defect X and the effect the HIPping process had on the overall dimensions of the healed inclusion, a smaller block of 2 by 1 by 1 inches was cutout from the larger block. The location of the defect in the smaller block was then pinpointed and the inclusion sliced perpendicular to its axis. Twenty 100-mil slices were produced and each cutting step consumed about 15 mils of material. Figure 41 shows how the slicing process was performed.

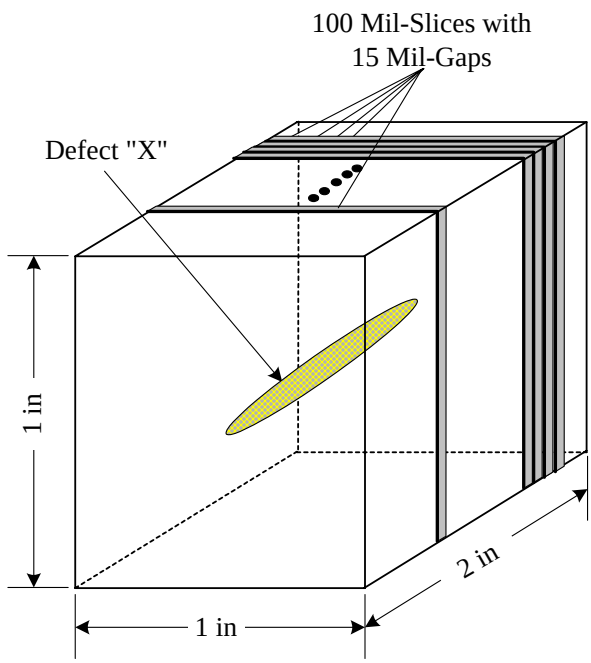

FIGURE 41. SLICING PROCESS PERFORMED ON DEFECT X PERPENDICULAR TO ITS AXIS TO PRODUCE TWENTY 100-mil SLICES WITH 15-mil GAPS

Once the slices were prepared, both eddy-current and acoustic microscopy imaging were performed on them. Figure 42 shows sample results from the eddy-current imaging, and figure 43 shows similar sample results from acoustic microscopy imaging. The eddy-current imaging maps the variation in electrical conductivity that is affected by the presence of nitrogen and its distribution throughout the sample. The images shown in figure 42 were taken using a 6-MHz, eddy-current probe with 4-mils liftoff and a scanned image with dimensions of 1.2 by 1.2 inches. The presence of the defect in the slice is very clear from the indications in these images; however, the spatial resolution is not good enough to allow accurate sizing of the inclusion. According to these images, the estimated maximum defect width is 10 mm, and the estimated maximum thickness is as 4 mm, which are reasonably close to the dimensions assumed in the simulation models.

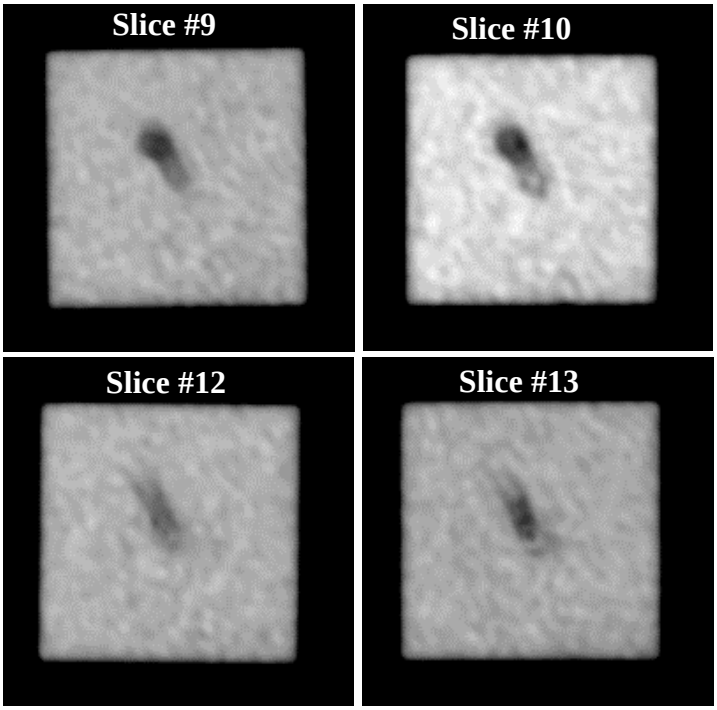

FIGURE 42. SAMPLE RESULTS OF THE EDDY-CURRENT IMAGING OF SOME OF THE SLICES FROM INCLUSION X

The acoustic microscopy images shown in figure 43 were collected using the Sonix acoustic microscope, using a Panametrics V324 (serial number 148627), 25 MHz, 0.25 inch in diameter, focused at the back wall of the specimen under consideration. The presence of the inclusion is clearly detected and some size information can be extracted. According to these images, the estimated maximum defect width is 7 mm, and the estimated maximum thickness is 1 mm. These estimates are significantly smaller than the dimensions assumed in the simulation models, which could explain why the defects where not observed in TOF data from the larger block. The overall length of the defect along its axis was calculated by counting the number of slices from when the first slice in which the defect appears to the last slice in which the defect is still detectable. There were a total of nine slices. Taking the slice thickness to be 100 mils and assuming only 15 mils in lost material in each cutting step, the estimated length of the inclusion is about 0.885 inch (about 22 mm). This value is larger than the length assumed in the simulations. It must be mentioned here that although the length of the defect along its axis is comparable between the experimental results and the simulation model, the other two dimensions of the inclusion seem to be much smaller than what was assumed and more reflective of the second simulation model that assumes a 15-mm-long and 1-mm-wide inclusion. The results from that simulation model clearly showed that no measurable effect would be detected for this case. Also, it should be emphasized that the actual inclusion size that can modulate the phase of the propagating UT wave is that of the region enriched by nitrogen (> 2% by weight). To more accurately determine this size, a metallurgical analysis was performed on some of these slices along with a chemical microprobe analysis.

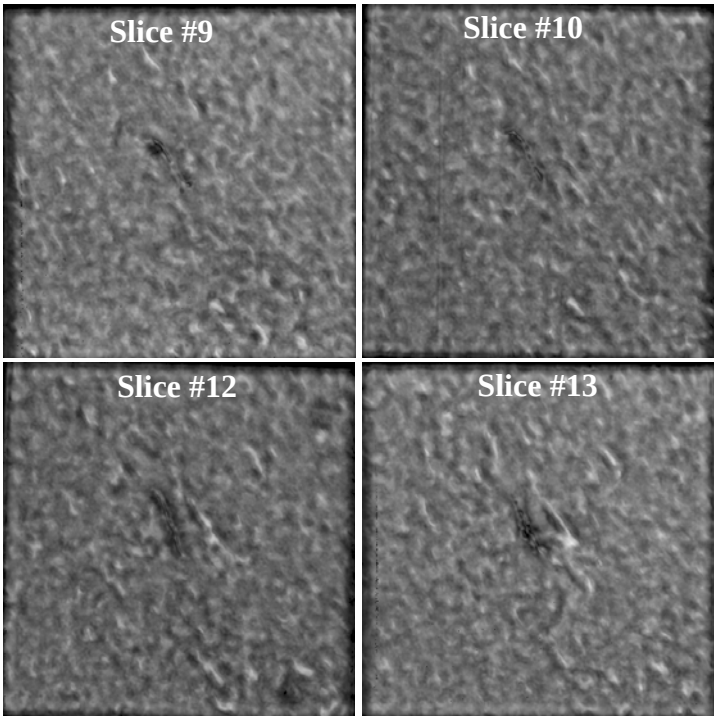

FIGURE 43. SAMPLE RESULTS OF THE ACOUSTIC MICROSCOPY IMAGING OF SOME OF THE SLICES FROM INCLUSION X

8.2 METALLURGICAL AND MICROPROBE ANALYSIS.

Of the 20 slices making up the block that contained the inclusion X, only slices 9 through 13 were characterized in the scanning electron microscope as to size, shape, and qualitative compositional differences. Size measurement results for the defect in each of the sampled cross sections is reported in table 5. Note that the thickness was not uniform, with nuggets at various positions along the width that were wider than most of the defect. The thickness of these nuggets defined the width dimension maxima in table 5. The general characteristics of all five defects were sufficiently similar, thus, it is necessary only to describe one. Slice 13 was selected for the characterization that follows.

TABLE 5. SIZE OF THE DEFECT IN EACH EXAMINED SLICE CROSS SECTION

Slice No.	9	10	11	12	13
Length	8.5 mm	7.6 mm	7.5 mm	7.7 mm	8.1 mm
Width	≤ 1.5 mm	≤ 1.4 mm	≤ 1.5 mm	≤ 1 mm	≤ 1 mm

In figure 44, note that there are no cracks or pores of sufficient size to serve as reflectors of the sonic signal; the thickness dimension is quite small, so even if the properties are different, the effect on the sound signal will be difficult to detect.

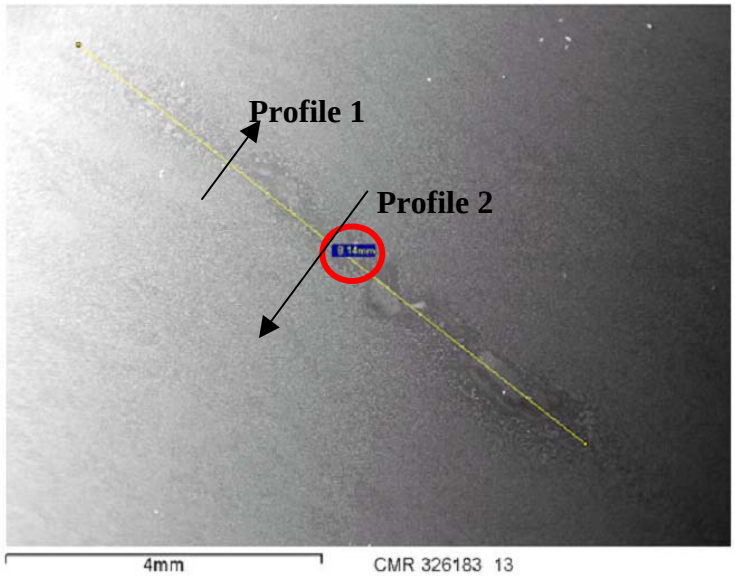

FIGURE 44. MICROSTRUCTURE FOR SLICE 13 SHOWING THE NONUNIFORM THICKNESS ALONG THE WIDTH OF ABOUT 8 mm

Further analysis of the region indicated in figure 44 by a red circle was carried out, as this region is distinguishable from other parts of the defect. Figure 45 is a slightly higher magnification view of that area showing a very nonuniform microstructure. It also clearly illustrates a gradient of microstructures. It is assumed that the core of the defect is represented by the mottled area. The core is highlighted by a black arrow. Figure 46 is an even higher magnification view of this area and a multiphase zone of the inclusion can clearly be seen.

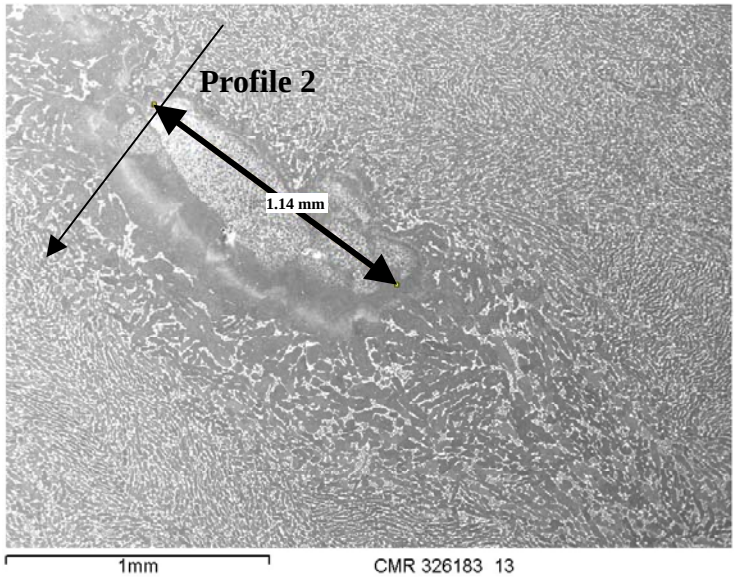

FIGURE 45. HIGHER MAGNIFICATION VIEW OF AREA CIRCLED IN FIGURE 44

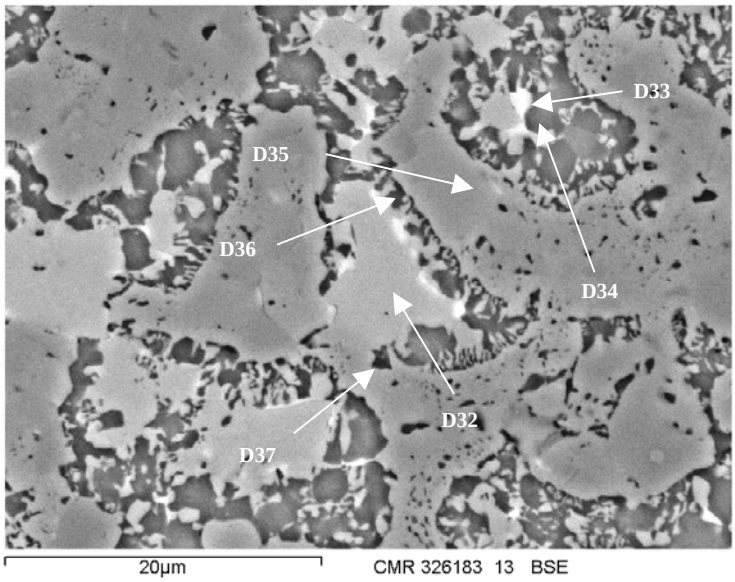

FIGURE 46. HIGH MAGNIFICATION, BACKSCATTERED ELECTRON IMAGE OF MOTTLED AREA SEEN IN FIGURE 45, HIGHLIGHTING AREAS WHERE ENERGY DISPERSIVE X-RAY ANALYSES WERE MADE

From the energy dispersive x-ray analyses (EDX) spectra of these areas compared to the EDX scan of the base material, it is possible to make some qualitative observations regarding the composition of the selected areas. Note that there is a wide variety of compositions within a small area of the core of this defect. For the most part, nitrogen is the dominant interstitial alpha stabilizer and the nominal alloy constituent contents are variable. Separate, a spread beam analysis of the mottled area revealed that this area had lower Al content and higher N content than the baseline alloy. This is consistent with nitrogen-stabilized hard alpha defects but not likely one originating from splatter ring oxidation due to the lower Al content. The splatter ring is generally characterized as being higher than nominal with respect to Al content. It is clear that this hard alpha is far from homogeneous in composition or structure so models of its behavior must account for its inhomogeneity. Selected microprobe traces were done on samples to quantify N content across the defect. For those run on slice 13, trace marks are shown on figure 44 with the results plotted in figures 47 and 48. From these figures, it is apparent that the N content in this defect is far from uniform, a situation not uncommon amongst other naturally occurring hard alpha defects. This nonuniformity is on a scale approaching the dimensions of the defect as well as on a smaller scale, as indicated in figure 46 and table 6. A quick review of hard alpha characteristics reported in the 1990 to 2001 time period shows N contents from 1.1% to 12%. (N = 8, avg. = 6.8%).

Based on figure 47, the width of the inclusion with any appreciable N content (> 0.2% by weight) can be estimated as 0.3 mm. If one actually considers that appreciable modulation of the sound, speed will occur only if the N content is higher than 1.0% by weight. Figure 48 shows very clearly that the width of the inclusion is less than 0.2 mm. These dimensions are much smaller than those used in the simulation models and indicate very clearly that the HIPping process collapsed the cavities in the voided hard alpha inclusion and left a very thin narrow

string running through the host material. Keeping these facts in mind, one can conclude that no phase modulation of the propagating longitudinal-wave front would be detectable in the original block that contained the defect, as the propagation width of the sound in the inclusion is a small fraction of the beam width and, hence, no indication of the defect would be observed in the TOF data as seen from the previous experimental results.

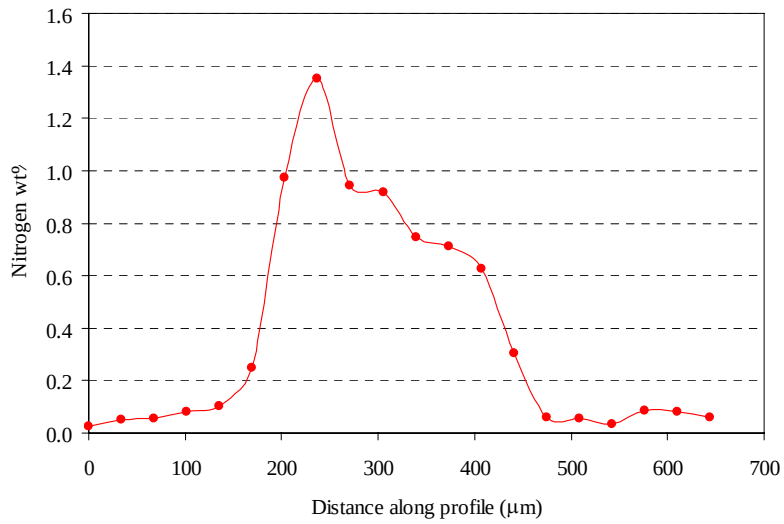

FIGURE 47. NITROGEN COMPOSITION TRACE (FROM MICROPROBE ANALYSIS) ACROSS DEFECT OF SLICE 13 ALONG PROFILE 1
(Microstructure is shown in figures 44 through 46.)

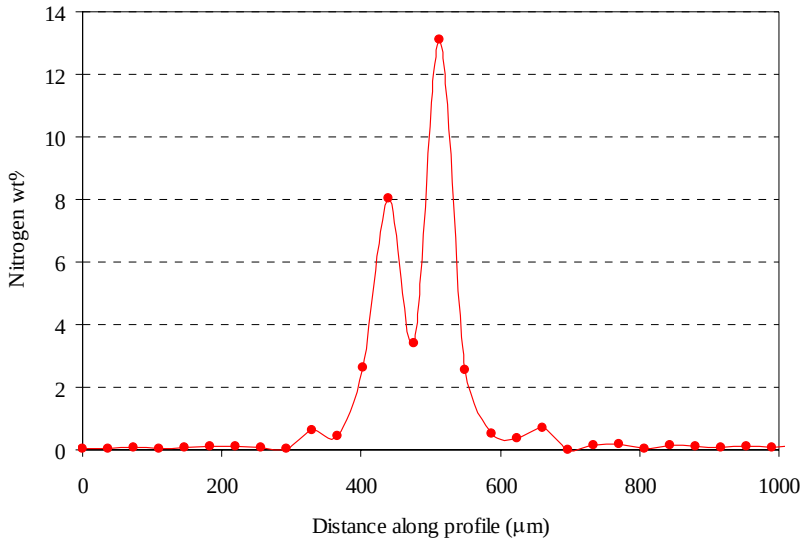

FIGURE 48. MICROPROBE TRACE ALSO FROM SLICE 13 ALONG PROFILE 2 SHOWING MUCH HIGHER N CONTENT THAN THE FIRST TRACE

TABLE 6. QUALITATIVE DIFFERENCES IN COMPOSITION WITH RESPECT TO THE BASE ALLOY COMPOSITION

	D32	D33	D34	D35	D36	D37
Al	0	N/A	+	none	+	--
Fe	0	+	+	N/A	N/A	N/A
V	0	+	+	0		0
N	+	0	+	++	+	++
C	0	0	+	+	+	+

Figure 49 shows combined traces of N and Al for slice 13. Note the apparent exclusion of the two elements. Al and N are both alpha stabilizers so there is no phase partitioning to explain this. A possible explanation is as follows. In the Ti-6Al-4V alloy manufacturing process, Al diffuses slowly through nitrogen-enriched alloy. This analysis indicates that the N enriched the titanium alloy early in the melting process, and the Al did not have a chance to diffuse through these regions. It is also clear that the air leak affected the material prior to the point in the process where complete alloying had occurred. The principal suspect is that the air leak occurred during primary melting. It was incompletely homogenized melt or more likely, the unmelted electrode that was most affected by the air leak.

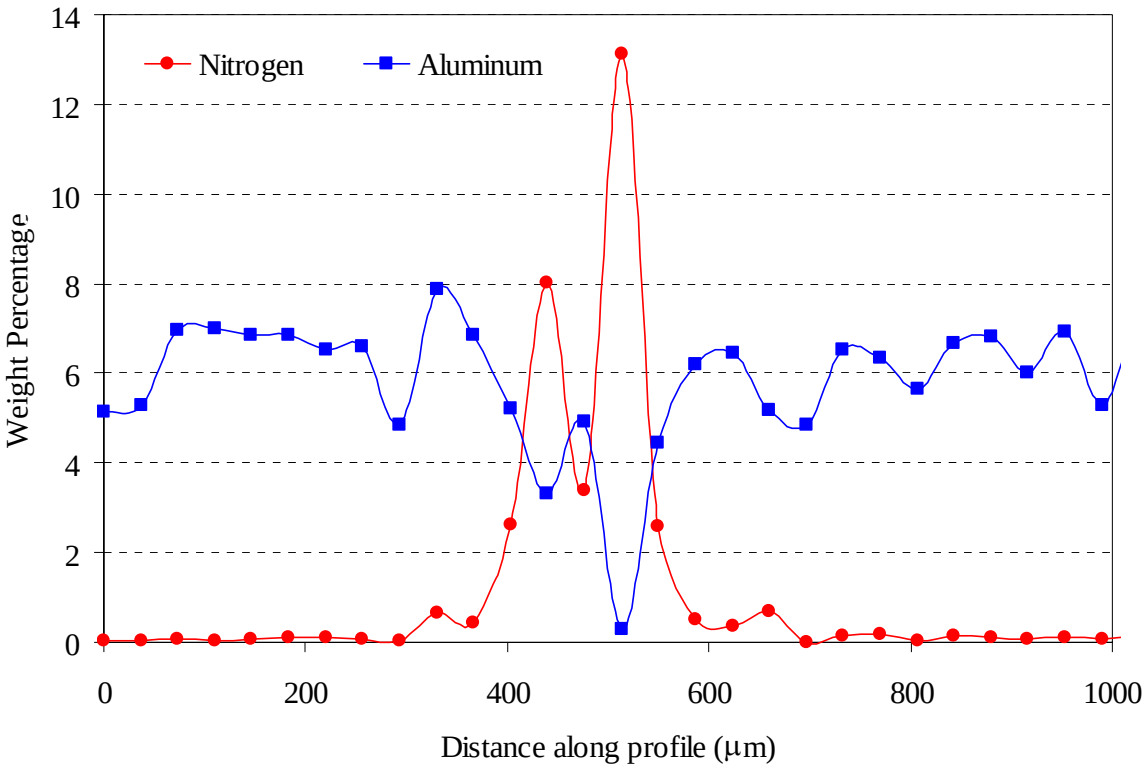

FIGURE 49. COMBINED TRACES OF N AND Al FOR SLICE 13 ALONG PROFILE 2
(Note the apparent exclusion of the two elements.)

9. SUMMARY.

Hard alpha inclusions are low-density, hard, brittle regions of spuriously high nitrogen and oxygen content that occur in titanium alloys. These inclusions are often cracked or include voids, which makes it much easier to detect by conventional NDT methods, including UT backscattering. However, the detection of uncracked/unvoided hard alpha inclusions represents a very significant challenge for UT NDT. Although every weight percent of N was found to increase the sound velocity by roughly 3%, therefore, the absolute acoustic impedance contrast is expected to be substantial (10%-15%), the actual SNR is badly limited by three adverse effects. First, the N content varies gradually towards the center of the inclusion; therefore, the reflected signal remains rather weak. Second, the shape of the inclusion is typically very irregular; therefore, the flaw signal is further reduced by random geometrical scattering effects. Third, the competing grain noise is frequently very high because of the often coarse microstructure of the surrounding material. As a result, the backscattered UT signal from the unvoided hard alpha inclusion is usually indistinguishable from the incoherent material noise based on its strength alone and the probability of its detection remains inherently low.

The objective of this program was to investigate the feasibility of a new UT NDT method aimed at detecting nonvoided hard alpha inclusions in titanium billets. As a working hypothesis, it was postulated that, in general, nonlinear elastic properties are more sensitive to the presence of interstitial (N, C, and O) elements that lead to higher hardness than the corresponding linear elastic properties. There are a great variety of nonlinear elastic parameters that could be exploited for NDE of hard alpha inclusions. The three nonlinear parameters that were investigated in details were chosen with special regard to the particular nonlinear NDE method that was used in this study, namely, thermally activated elastography. These nonlinear parameters include the TEC, the thermal coefficient of sound velocity (ATC), and the stress coefficient of sound velocity (AEC). Of course, these nonlinear parameters are mutually interrelated and are all dependent on the higher-order elastic moduli of the material.

All three nonlinear parameters were experimentally measured in order to assess the contrast in these properties between an unvoided hard alpha inclusion and the titanium host material that will ultimately determine the feasibility of such an inspection technique. Based on the measurements, the direct thermal expansion effect and the thermally induced acoustoelastic effect are all practically negligible relative to the acoustothermal velocity change. This last parameter was found to be rather sensitive to changes in N content (for simplicity, these coefficients were not corrected for thermal expansion, which represents a smaller effect than the other experimental uncertainties in the measurements). Both the longitudinal and shear ATCs are negative, i.e., the velocities decrease with increasing temperatures. Furthermore, the longitudinal coefficient decreases while the shear coefficient increases with increasing nitrogen content. The behavior of the shear coefficient is rather surprising in light of the fact that brittle materials usually exhibit reduced elastic nonlinearity, which should decrease the temperature dependence of the shear velocity too. One possible explanation is that shear wave propagation is more affected by the presence of microporosity and other microstructural imperfections, which accompany the increase in N content. This porosity is also believed to be responsible for the dramatically reduced mechanical strength of the nitrogen-enriched specimens and for the fact that specimens of the highest N content could not be tested by UT means at all. It is likely that this porosity has also adversely influenced the longitudinal acoustothermal measurements in

specimens of higher than 3% N content; therefore, additional efforts to increase the accuracy and reliability of such experiments are needed in future efforts.

From the results presented previously (see equation 15), it was concluded that the acoustothermal effect is the dominant effect amongst the three measured nonlinear parameters. For a 50°C change in temperature, it was predicted that there would be approximately 0.65% change in velocity, which is less than the previously estimated upper limit of 1.0% velocity change. Simulation models using the finite difference wave propagation simulation software, Wave2000Pro, showed very clearly that a cigar-shaped, unvoided hard alpha inclusion, 15 mm in length and 4 mm in width, in titanium would produce a peak shift in the longitudinal UT wave signal of about 11 nsec, which can be readily measured in the laboratory. This is of course subject to the validity of the assumptions about the actual inclusion, which include (1) the size of the defect used in the simulations is appropriate and representative of real inclusions, (2) the sound velocity in TiN increases by roughly 3% with each weight percent of nitrogen, and (3) the shape of the inclusion used in the simulations is representative of the actual defects.

Although preliminary feasibility (at least in a laboratory environment) has been predicted using the simulation models, the real test is to verify these predictions with experimental data from real unvoided hard alpha inclusions in titanium. The need for real unvoided hard alpha inclusion specimens in titanium alloys became the most important factor in the experimental verification process. To that end, two types of specimens were obtained from various sources during the course of the program.

A Ti-6Al-4V specimen with three synthetic cylindrical inclusions, manufactured using one of the methods indicated, was obtained from the NDE branch at Wright-Patterson Air Force Base in Dayton, OH. This block was intended for use in the technique validation experiments with the assumption that the inserted inclusions are representative of the condition of an unvoided hard alpha inclusion in Ti-6Al-4V. After the initial inspection of the block using backscattered UT inspection, it became very evident that this artificial inclusion specimen is not representative of a case of unvoided hard alpha inclusions in titanium alloys, and the block was ruled out from any future investigations. Several factors can account for the very strong UT response received from these synthetic inclusions. First, the interface between the inclusions and the titanium host materials is sharp in terms of the change in N content, which is not the case for a naturally occurring unvoided hard alpha inclusion. Second, the porosity associated with such inclusions (specially the ones with the high N content) may contribute to a higher than expected UT signal. And finally, the questionable diffusion interface between the inclusion and the host material may result in such a high signal if the inclusion is not completely bonded to the host material. For all these reasons, this specimen was deemed to be not representative of naturally occurring hard alpha inclusions in titanium alloys and, therefore, was not used in any further activities in this program.

To generate samples that might be more representative of real unvoided hard alpha inclusions in titanium, it was decided to acquire some voided hard alpha inclusion samples and put them through a HIPping process to close the voids, assuming that will preserve the overall dimensions of the inclusion. For the purposes of this program, several billet pieces having about 15 indications left over from the CBS were obtained from the ETC team. A number of these

indications were verified again in these billets using an MZI procedure, and their locations in the respective billets were pinpointed. In particular, a 25.75-inch-long billet section (B2W2C) containing two indications (X and D) was extensively studied. After precisely locating the two defects in the billet, they were cut out from the billet material to form two blocks with dimensions of 2 by 2 by 2.82 inches and 2 by 2.73 by 2.82 inches, respectively. The presence of the inclusions in the blocks were again verified and the two blocks were HIPped at 1650°F and 30 ksi pressure for 5 hours. UT inspection of these blocks after HIPping showed no indication of the inclusions, which was expected, and indicated that the HIPping did actually heal all the voids within these inclusions. What was surprising in the results obtained, despite very careful measurements, the fact that there were no indication of these inclusions in the TOF data in contradiction with the prediction from the simulations. This led to questions concerning the nature of the inclusions and how representative they were of real unvoided hard alpha inclusions. There were three assumptions about the inclusion type in the simulation models relating to the size, shape, and nature of velocity modulation it would produce. These assumptions were mentioned above. Assumptions two and three have been proven to be valid in this and other studies. The first assumption that relates to the size of the inclusion was very questionable and was proven (in this study) to be invalid for the unvoided hard alpha specimens generated from the CBS voided hard alpha specimens through the HIPping process. Although the length of the defect along its axis is comparable between the experimental results and the simulation model, the other two dimensions of the inclusion seem to be much smaller than what was assumed and more reflective of the second simulation model that assumes a 15-mm-long and 1-mm-wide inclusion. The results from that simulation model clearly showed that no measurable effect would be detected for this case. Also, it should be emphasized that the actual inclusion size that can modulate the phase of the propagating UT wave is that of the region enriched by N (> 2% by weight), which was shown through metallurgical and microprobe analyses to be much less than 1 mm in width. Based on figure 47, the width of the inclusion with any appreciable N content (> 0.2% by weight) is estimated as 0.3 mm. With consideration that appreciable modulation of the sound speed will occur only if the nitrogen content is higher than 1.0% by weight, figure 48 shows very clearly that the width of the inclusion is less than 0.2 mm. These dimensions are much smaller than those used in the simulation models and indicate very clearly that the HIPping process collapsed the cavities in the voided hard alpha inclusion and left a very thin narrow string of unvoided hard alpha material running through the host material. Keeping these facts in mind, one can conclude that no phase modulation of the propagating longitudinal wave front would be detectable in the original block that contained the defect, as the propagation distance of the sound in the inclusion is a small fraction of the overall propagation distance and, hence, no indication of the defect would be observed in the TOF data as seen from the experimental results.

Although these results were rather disappointing, they do not constitute evidence that the proposed thermal elastography technique is not feasible. The predictions based on the results from the experimental measurements of the ATC show very clearly that the effect is measurable. However, the lack of specimens representing a real unvoided hard alpha inclusion in titanium of the type and size shown in figure 2 has made it impossible to demonstrate this feasibility practically in the laboratory or at an inspection facility. If such samples do exist, the information included in this report can be used for such a practical demonstration of the technique capability.

10. RECOMMENDATIONS.

The acoustoelastic measurements were not performed on the brittle TiN specimens because they were too small for the MTS and their mechanical strength was highly questionable. The 1-inch-long specimens could most likely be tested in compression, which would require an extensive setup preparation. Since it was shown earlier that the relative contributions of the thermal expansion and AECs were small compared to the ATC, it was not considered a serious limitation that the TiN specimens could not be tested in the MTS.

In light of the research findings, further improvement of the acoustothermal measurements that were found to be crucial for the feasibility of the thermalelastographic detection of nonvoided hard alpha inclusions in titanium alloys is desired. As mentioned before, these tests are tedious and complicated, which can often lead to spurious artifacts and, ultimately, incorrect results. Many precautions have been taken to ensure that the tests are repeated in a similar manner. Intrinsic measurement uncertainties include electrical noise, mechanical vibrations, thermal instability, long-term drift, etc. Possibly, the lack of sufficient reproducibility is caused by aging of the UT transducers and imperfect coupling to the specimens, while instrument anomalies and imperfections appear to be under control. Many tests have been discarded because of spurious spikes in the data, noise from the MTS when in use by someone else, or a nonlinear velocity versus temperature curve. Explaining why a particular test went wrong is nearly impossible, but knowing that it did go wrong is easy. However, a study to understand the effect that different amounts of couplant, different water levels, and different transducers may have on the stability and sensitivity of the measurements would be quite beneficial.

The longitudinal measurements seem to be easier than the shear measurements. The water is allowed to air-cool from 80°C to room temperature, whereas the water is cooled by the chiller to 5°C in the shear measurements. This factor seems to produce a noticeable curvature in most of the shear plots at the same point in the temperature range. However, this method must be used because of the viscosity loss of shear couplants. Evaluating the possibility of using shear waves to perform the thermal elastographic detection of unvoided hard alpha inclusions in titanium should be considered in future activities.

Finally, a future activity to try to secure unvoided hard alpha inclusion specimens of the type and size that is representative of real naturally occurring unvoided hard alpha inclusions in titanium should be considered. These specimens can be used to demonstrate (at least in the laboratory environment) the actual feasibility of the technique under consideration in this effort. Investigation of the possibility of producing such unvoided hard alpha samples if no such samples are currently in existence is also recommended. Understanding how such inclusions form without cracking and voiding is critically needed to produce such samples. If such samples do exist, the information included in this report can be used to practically demonstrate the thermal elastographic technique capability.

11. REFERENCES.

1. FAA Advisory Circular 33.15-1, "Manufacturing Process of Premium Quality Titanium Alloy Rotating Engine Components," September 22, 1998.

2. "United Airlines Flight 232 McDonnell Douglas DC-10-10 Sioux Gateway Airport, Sioux City, Iowa," July 19, 1989, NTSB Report Number, AAR-90-06, November 1, 1990.

3. Brasche, L.J.H. and Buck, O., "Nondestructive Methods for Determination of Mechanical Properties of Aluminum and Titanium Alloys," *Review of Progress in Quantitative Nondestructive Evaluation*, Vol. 10B, 1991.

4. Chan, K.S., Perocchi, L., and Leverant, G.R., "Constitutive Properties of Hard-Alpha Titanium," *Metallurgical and Materials Transactions*, Vol. 31A, 2000.

5. Bogan W.W., "Metallurgical Evaluation: RMI 2XVAR Ti64 Heat 883588 Hard Alpha," Internal ETC Letter Report, April 27, 1995.

6. Brasche, L.J.H., Chiou, T., Thompson, B., Smith, K., Meeker, W., Margetan, F., Paul Panetta, P., Chenail, R., Galli, F., Umbach, J., Raulerson, D., Degtyar, A., Bartos, J., Copley, D., McElligott, B., Howard, P., and Bashyam, M., "Contaminated Billet Study," FAA report DOT/FAA/AR-05/16, September 2005.

7. Bartos, J.L., Copley, D.C., Gilmore, R.S., and Howard, P.J., "Advanced Ultrasonic Inspection Techniques for Titanium Billet Materials," *Titanium '95: Science and Technology*, Vol. 2, 1996.

8. Leverant, G.R., McClung, R.C., Wu, Y.-T., Millwater, H.R., Riha, D.S., Enright, M.P., Chell, G.G., Chan, K.S., McKeighan, P.C., Gorelik, M., Fischer, C., Lehmann, D., Green, K., Bartos, J., Howard, N., and Srivatsa, S., "Turbine Rotor Material Design," FAA Report DOT/FAA/AR-00/64, December 2000.

9. Giglioti, M.F.X., Gilmore, R.S., and Perocchi, L.C., "Microstructure and Sound Velocity of Ti-N-O Synthetic Inclusions in Ti-6Al-4V," *Metallurgical and Materials Transactions*, Vol. 25A, 1994.

10. See www.matweb.com.

11. Ruiz, A. and Nagy, P.B., "SAW Dispersion Measurements for Ultrasonic Characterization of Surface-Treated Metals," *Instrumentation, Measurement and Metrology*, Vol. 3, 2003.

12. Margetan, F.J., Gigliotti, M., Brashe, L., and Leach, W., "Fundamental Studies: Inspection Properties for Engine Titanium Alloys," FAA report DOT/FAA/AR-02/114, December 2002.